Atmospheric Research 275 (2022) 106223

Contents lists available at ScienceDirect

Atmospheric Research

journal homepage: www.elsevier.com/locate/atmosres

Impact of ocean-atmosphere coupling on present and future Köppen-Geiger climate classification in Europe

Rafael Falquina [a,*], Alba de la Vara [b,d,f], William Cabos [c], Dmitry Sein [e], Clemente Gallardo [b]

[a] Universidad Complutense de Madrid, Facultad de Ciencias Físicas, Av. Complutense s/n, 28071 Madrid, Spain
[b] Universidad de Castilla La Mancha Facultad de Ciencias Ambientales, Av. Carlos III s/n, 45071 Toledo, Spain
[c] Universidad de Alcalá, Departamento de Física, Universidad de Alcalá, Alcalá de Henares, Madrid, Spain
[d] Universidad Politécnica de Madrid, E.T.S.I. Industriales, Departamento de Matemática Aplicada a la Ingeniería, C/ José Gutiérrez Abascal, 2, 28006 Madrid, Spain
[e] Alfred Wegener Institute for Polar and Marine Research, Bremerhaven, Germany
[f] Senior Europa S.L.–Kveloce I + D + i: Plaza de la Reina 19, Escalera A, 1°, 46003 Valencia, Spain

ARTICLE INFO

Keywords:
Climate change
Climate classification
Regional climate model
Ocean-atmosphere coupling

ABSTRACT

The effect of air-sea coupling in the simulation of the European climate is assessed through a climate type classification that uses surface temperature and precipitation from a regional atmosphere-ocean coupled model and from its atmospheric component. The atmospheric setup in both models is the same, differing only in the representation of the oceanic fields. The simulations cover the present and future-time climate under the RCP8.5 CMIP5 scenario. Climate type distributions obtained from both coupled and uncoupled simulations are similar to those obtained from ERA5 for the 1976–2005 period. Both models simulate colder climate types for present-time in southern and northeastern regions compared to ERA5, possibly due to a weaker influence of the Atlantic circulation, and drier climate types in some western Mediterranean areas. Also, for present-time coupling leads to more humid winters (relatively drier summers) in some zones of north Spain and south France, and drier climates in some western Mediterranean spots. Based on simulations with these models under the RCP8.5 scenario, we find that by the end of the 21st century (2070–2099) the climate type distribution changes in more than 50% of the domain. While both models project the reduction of regions with cold climate types and the expansion of those with hot summers and hot arid climate types, these changes affect a larger area in the coupled simulation. These differences may be related to a drier signal in the coupled simulation, especially during summer, due to the influence of colder surface water in the North Atlantic Ocean and the Mediterranean Sea. Using a climate classification to evaluate the annual cycles of the simulated temperature and precipitation data provides a novel insight into the impact of air-ocean coupling on the representation of the climate, and consequently into the simulated impact on ecosystems and human activities in Europe.

1. Introduction

For many years now, downscaling of data derived from reanalyses, Global Climate Models (GCMs) or Earth System Models (ESMs) using Regional Climate Models (RCMs) has been used to increase climate data spatial resolution. This technique has a variety of applications (Castro et al., 2005; Rockel, 2015), including local or regional climate change assessment (e.g., Barredo et al., 2020; Komurcu et al., 2018; Mathis et al., 2013; Xue et al., 2014). The finer mesh of the RCMs allows for a better resolved orography or local gradients (e.g., Cabos et al., 2019; Pontoppidan et al., 2017; Rummukainen, 2016; Takemi and Ito, 2020; Tiwari et al., 2014; Xu et al., 2018). Also, the importance of using high-spatial resolution RCMs for regional analyses based on momenta beyond mean values is shown in the literature (e.g., Domínguez et al., 2013; Gómez et al., 2016). For an assessment of the applications of RCMs over Europe see e.g., the perspective of EURO-CORDEX (Jacob et al., 2020). High spatial resolution regional models are also important for other regions of the world, see for example the different results of the Coordinated Regional Climate Downscaling Experiment (CORDEX) initiative in (Allam et al., 2020; Cabos et al., 2019; Giorgi and Gutowski, 2015; Giorgi et al., 2021).

RCMs use atmospheric and oceanic boundary conditions from reanalyses or GCM/ESM and, generally, the sea-surface temperatures (SSTs) used as lower boundary conditions, as well as other atmospheric

* Corresponding author.
E-mail address: rfalquin@ucm.es (R. Falquina).

https://doi.org/10.1016/j.atmosres.2022.106223
Received 1 December 2021; Received in revised form 17 March 2022; Accepted 26 April 2022
Available online 30 April 2022

Table 1
Model setup used in ROM.

Driving global climate model	MPI-ESM
Regional atmosphere model	REMO
Horizontal atmospheric resolution	0.25 degrees
Vertical atmosphere resolution	27 hybrid vertical levels (radiative upper boundary)
Coupler	OASIS 3.0 (3-h coupling time step)
Global ocean model	MPIOM
Ocean horizontal resolution	5–100 km
Ocean vertical resolution	47 levels, between 16 m (shallowest) and 650 m (deepest) thickness

fields used as lateral boundary conditions, are defined in a coarser mesh (e.g., Giorgi and Gutowski, 2015). Regional Atmosphere-Ocean Coupled Models (RAOCMs) provide the SST in a usually much finer resolution, thus accounting better for the impact of the ocean on the atmosphere. This may be important in regions exposed to different air and ocean masses, since regional models generate their own dynamics, reducing the dependency on the information provided by the coarser global model used to force them, especially far away from the boundaries (e.g., Cabos et al., 2019).

Climate classifications are algorithms that group locations with climate similarities into classes, each class being defined as a climate type (Jacobeit, 2010). The climate types for a certain classification are usually mapped to some other characteristic shared by the locations in each class, e.g., vegetation type, solar radiation, water availability (Allam et al., 2020), thermal comfort (Wan et al., 2010), suitability for a certain crop (Tonietto and Carbonneau, 2004), biodiversity (Metzger et al., 2013), habitat distribution (Guisan and Zimmermann, 2000), paleoclimate analyses (Willmes et al., 2017) or climate change (Belda et al., 2016) among others. The selection of an appropriate climate classification depends on the question being tackled. We distinguish subjective classifications based on arbitrary thresholds and criteria related to vegetation, like those from Köppen (Köppen, 1936), Köppen-Geiger (Geiger, 1961), Thornthwaite (Thornthwaite, 1948), Trewartha (Trewartha and Horn, 1980), classifications based on global atmospheric patterns and air masses distributions (e.g., Borchert, 1953) and objective climate classifications specially defined for a specific analysis (e.g., Falquina and Gallardo, 2017; Forsythe et al., 2015; Zscheischler et al., 2012). Climate classifications are therefore valuable for analyzing meteorological stations or reanalysis data (Forsythe et al., 2015; Keller and Wahl, 2021) and model output (Belda et al., 2016; Gallardo et al., 2013; Lohmann et al., 1993; Tapiador et al., 2019a; Tapiador et al., 2019b) in terms of climate types. The huge amount of data generated by meteorological stations and models can be downsized and make it more easily understandable by using clustering techniques and criteria provided by climate classifications. The Köppen-Geiger (K-G) climate classification provides a simple way to downsize and encode gridded observational data, model outputs or reanalyses into ecologically-significant classes, i.e., the K-G climate types. Therefore, climate types are useful to understand how reanalyses, climate model results and their differences could impact ecological systems and human activities. In particular, since the K-G classification climate types are related to vegetation types, this can be useful to determine if the air temperature and precipitation differences induced by air-sea coupling entail meaningful differences for environmental studies.

Previous works have demonstrated the importance of high spatial resolution for climate classification in areas with a complex orography and also to improve the simulation of the atmosphere and ocean circulation, see e.g., the applications of Skalák et al. (2018) for Central Europe climate change analysis, Andrade and Contente (2020) for the Iberian Peninsula, Barredo et al. (2020) for European Alpine Tundra and Allam et al. (2020) for Mediterranean hydrology analyses. The main objectives of this work are (i) to examine the sensitivity of present-time K-G climate types distribution in Europe to air-sea coupling processes and (ii) to understand how these processes affect the distribution of K-G types over Europe by the end of the 21st century assuming the Representative Concentration Pathway 8.5 (RCP8.5) scenario of the Coupled Model Intercomparison Project 5 (CMIP5). To that end, we use the results of a set of historical and future-time experiments performed with the ocean-atmosphere regionally coupled model ROM (Sein et al., 2015) and its stand-alone atmospheric component REMO (Jacob, 2001). The selected domain includes most of Europe. In ROM, the ocean model MPIOM (Jungclaus et al., 2013; Marsland et al., 2003) is global, which avoids problems associated with ocean open boundary conditions and allows for a better representation of the influence of the Atlantic water in the Mediterranean (Parras-Berrocal et al., 2020). MPIOM is coupled to the atmosphere over the area covered by the atmospheric model REMO. Different to many previous works, in our setup, the atmospheric model domain includes the North Atlantic and the Mediterranean Sea. This allows us to study the effect of the air-sea coupling of North Atlantic and Mediterranean on the European climate simultaneously, which is important because most European areas are subjected to the influence of the Atlantic and/or Mediterranean oceanic and atmospheric circulation (Sein et al., 2020; Jacob et al., 2014).

This work is structured as follows. In Section 2 the model setup, dataset used for the validation and the methods applied for the K-G classification are described. In Section 3, the results from the K-G classification obtained for the present-time experiments from REMO and ROM are compared to those derived from a reanalysis, thus assessing the impact of the air-sea coupling on the resulting climate classification. Also, the climate change signals from ROM and REMO are compared. A summary and the conclusions are given in Section 4.

2. Data and methodology

2.1. Model setup and reference dataset

The numerical experiments analyzed in this work were carried out with the regionally ocean-atmosphere coupled model ROM (Sein et al., 2015) and its stand-alone atmosphere component REMO (Jacob, 2001). The two models have been extensively used to study the regional climate (e.g., Cabos et al., 2020; Jiménez-Guerrero et al., 2013) and the climate change signal (e.g., Darmaraki et al., 2019; Parras-Berrocal et al., 2020; Sein et al., 2020; de la Vara et al., 2021) of different regions of the world.

REMO is based on the regional atmosphere Europe model of the German Weather Service (Majewski, 1991), with the physical parameterizations taken from the global climate models ECHAM4 (Roeckner et al., 1996) and ECHAM5 (Roeckner et al., 2003). It uses a rotated grid with its equator in the center of the model domain, to avoid largely different grid sizes near the poles. In REMO most of the prognostic variables are relaxed towards the values of the forcing data in the eight outer rows of the grid (Davies, 1976). A radiative upper boundary condition is applied (Klemp and Durran, 1983). In the simulations analyzed in this work, REMO is run with a uniform horizontal resolution of 0.25° in a rotated grid and 27 hybrid vertical levels. The atmospheric domain used in this study includes the Mediterranean Sea and the North Atlantic Ocean, which allows us to gain insight into the influence of both in the European climate signal.

The Max Planck Institute Ocean Model MPIOM (Jungclaus et al., 2013; Marsland et al., 2003), the oceanic component of ROM, has an orthogonal curvilinear grid that allows a maximum resolution of 5 km (eddy permitting) near the Iberian Peninsula and around 100 km in the southern seas within the model domain. It has 47 unevenly spaced vertical levels, with a thickness starting at 16 m in the shallowest level and increasing up to 650 m at the deepest level. In MPIOM the water exchange in the Gibraltar and Dardanelles straits is explicitly simulated in a consistent way, allowing us to consider the crossed influence between the North Atlantic, Mediterranean and Black seas. Both REMO

Table 2
Experiments nomenclature. ROM ocean-atmosphere coupled model is described in (Sein et al., 2015); REMO is the stand-alone atmosphere component of ROM (Jacob, 2001); boundary conditions are taken from CMIP5 simulations performed with the low-resolution version of MPI-ESM (Giorgetta et al., 2013).

	REMO	ROM
Present-time (1976–2005)	REMOH	ROMH
Scenario RCP8.5 (2070–2099)	REMO85	ROM85

Table 3
Köppen-Geiger climate types found in the domain. For a complete list of types see (Kottek et al., 2006).

Climate type label	Climate type name
BWh	Hot desert
BWk	Cold desert
BSh	Hot semi-arid (steppe)
BSk	Cold semi-arid (steppe)
Cfa	Fully humid temperate, hot summer (humid subtropical)
Cfb	Fully humid temperate, warm summer (temperate oceanic)
Cfc	Fully humid temperate, cold summer (subpolar oceanic)
Csa	Temperate, with dry hot summer (hot summer Mediterranean)
Csb	Temperate, with dry warm summer (warm summer Mediterranean)
Dsb	Continental, with dry warm summer
Dsc	Continental, with dry cold summer (subarctic)
Dfb	Fully humid continental, with warm summer
Dfc	Fully humid continental, with cold summer (subarctic)
ET	Tundra

and MPIOM are hydrostatic and solve the Navier–Stokes equations using the Boussinesq approximation and are coupled via the OASIS3 coupler (Valcke, 2013). Other components of ROM, as the Hamburg Ocean Carbon Cycle (HAMOCC) model (Maier-Reimer et al., 2005), the hydrological discharge (HD) model (Hagemann and Dümenil-Gates, 1998; Hagemann and Gates, 2001), the soil model of REMO (Rechid and Jacob, 2006) and a dynamic thermodynamic sea ice model (Hibler, 1979) are run as REMO or ROM modules. Table 1 summarizes the model's setup.

Boundary conditions for the simulations are taken from the historical and RCP8.5 CMIP5 scenario simulations performed with the low-resolution version of the Max Planck Institute Earth System Model (MPI-ESM) (Giorgetta et al., 2013). The experimental setup is based on previous works (Cabos et al., 2017; Cabos et al., 2020; de la Vara et al., 2021), where the reader can find more details. The nomenclature that will be used from this point onwards to refer to the different REMO and ROM experiments is presented in Table 2. The historical data available extends from 1950 to 2005, but we select the 1976–2005 period for the present-time validation. Similarly, the RCP8.5 experiment extends from 2006 to 2099, but only the 2070–2099 period is selected for this study.

To validate the present-time results we use the European Centre for Medium-Range Weather Forecasts (ECMWF) Reanalysis 5th Generation (ERA5) dataset (Hersbach et al., 2020). ERA5, the newest global reanalysis of ECMWF, is produced with the forecasts of ECMWF's atmospheric model (version CY41R2) and a 4D-Var data assimilation system. Its horizontal resolution is approximately 28 km in our domain. ERA5 has been widely used as the reference reanalysis for global and Europe climate studies (e.g., Hirschi et al., 2011; Lavender et al., 2021; Lorenz et al., 2019; Qiu et al., 2021). ERA5 is preferred to meteorological station gridded datasets, like *E*-OBS (Haylock et al., 2008), because the underlying observational network for precipitation is poor in some areas of Europe, especially in Spain and the Balkans in our domain, and the fitting scheme produces data lacking spatial detail (Hofstra et al., 2009; Jiménez-Guerrero et al., 2013). This drawback is overcome in ERA5 by using a measurements best-fit instead of a simple fit-to-data approach. However, ERA5 also presents known issues (see e.g., section 10.2 of Hersbach et al. (2020) and Keller and Wahl (2021)) that we will consider in the discussion.

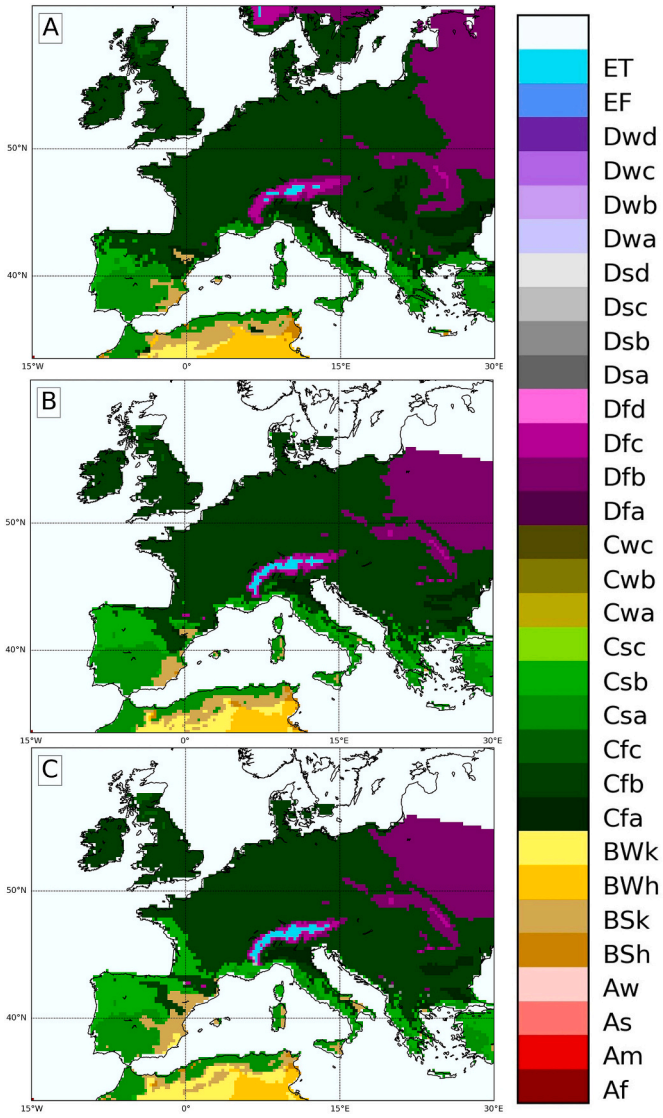

Fig. 1. Köppen-Geiger classification for 1976–2005. A ERA5; B REMOH; C ROMH.

E-OBS 22.0e data and ERA5 monthly averaged data on single levels are obtained from the Copernicus Climate Data Store (CDS). Thorough information about both datasets can be found in the ECMWF CDS dataset documentation, in Hersbach et al. (2020) and in Haylock et al. (2008). The orography for the REMO/ROM models and for the ERA5 dataset can be seen in Supplementary Material Fig. S.6.

2.2. K-G classification, data interpolation and climate similarity scores

In this work we use the K-G classification, which has been adopted in similar studies including the assessment of the global (Beck et al., 2018; Chen and Chen, 2013; Rubel and Kottek, 2010), regional and local environmental impact of climate change (Barredo et al., 2020; Dubreuil et al., 2019; Zeroual et al., 2019). Initially proposed by Köppen (Köppen, 1936) and later developed by Geiger (Geiger, 1961), it is based on five groups of vegetation (equatorial zone (A), arid zone (B), warm temperate zone (C), snow zone (D) and polar zone (E)), sub-classified depending on precipitation and air temperature, as described in the Supplementary Material (Table S.1). In our study we closely follow the classification scheme described by Kottek et al. (2006). Table 3 lists the

Table 4
Number (%) of cells per K-G climate type ($N = 8672$).

K-G Climate type	ERA5 (1976–2005)	REMOH (1976–2005)	ROMH (1976–2005)	REMO85 (2070–2099)	ROM85 (2070–2099)
BSh	42 (0.5%)	39 (0.4%)	22 (0.3%)	383 (4.4%)	507 (5.8%)
BSk	332 (3.8%)	304 (3.5%)	369 (4.3%)	159 (1.8%)	533 (6.1%)
BWh	265 (3.1%)	192 (2.2%)	196 (2.3%)	598 (6.9%)	691 (8.0%)
BWk	110 (1.3%)	207 (2.4%)	318 (3.7%)	36 (0.4%)	81 (0.9%)
Cfa	565 (6.5%)	238 (2.7%)	211 (2.4%)	1017 (11.7%)	772 (8.9%)
Cfb	4702 (54.2%)	4575 (52.8%)	4369 (50.4%)	3937 (45.4%)	3678 (42.4%)
Cfc	6 (0.1%)	21 (0.2%)	23 (0.3%)	0 (0.0%)	0 (0.0%)
Csa	1221 (14.1%)	1143 (13.2%)	934 (10.8%)	2257 (26.0%)	1918 (22.1%)
Csb	247 (2.8%)	583 (6.7%)	833 (9.6%)	222 (2.6%)	421 (4.9%)
Dfb	1033 (11.9%)	1202 (13.9%)	1220 (14.1%)	38 (0.4%)	38 (0.4%)
Dfc	123 (1.4%)	108 (1.2%)	97 (1.1%)	21 (0.2%)	22 (0.3%)
Dsb	0 (0.0%)	2 (0.0%)	5 (0.1%)	3 (0.0%)	7 (0.1%)
Dsc	0 (0.0%)	0 (0.0%)	4 (0.0%)	1 (0.0%)	4 (0.0%)
ET	26 (0.3%)	58 (0.7%)	71 (0.8%)	0 (0.0%)	0 (0.0%)

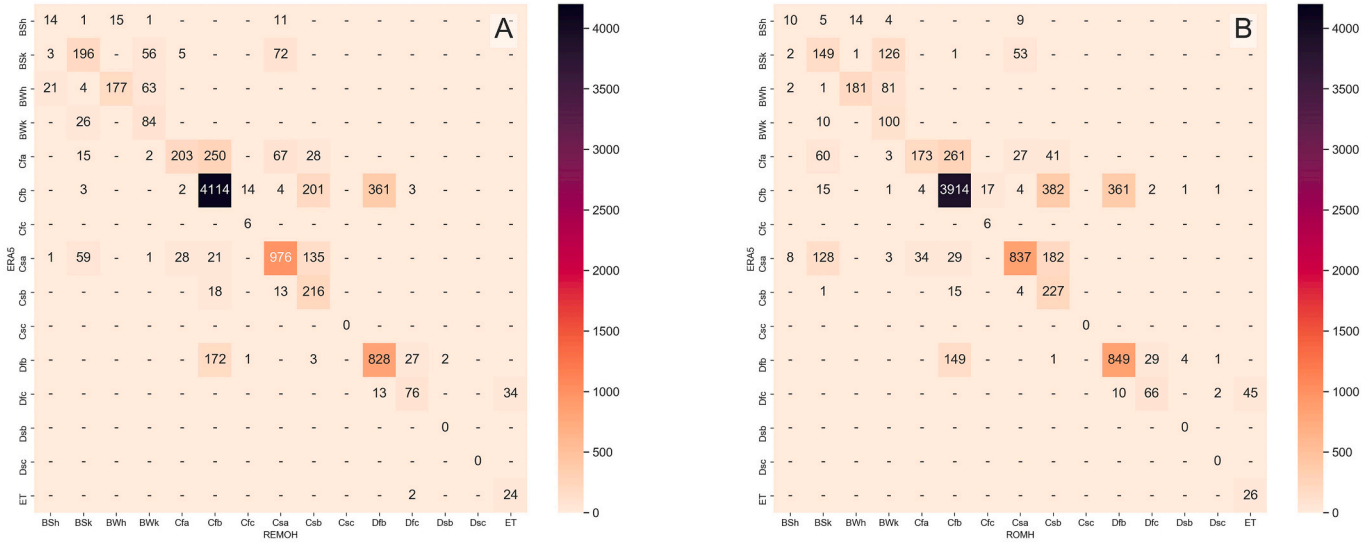

Fig. 2. Climate types matching matrix: A ERA5 vs REMOH; B ERA5 vs ROMH.

14 K-G climate types found for the domain analyzed in this work, although Cfc, Dsb and Dsc are barely present in a few cells and can be ignored thereafter.

To allow for a direct comparison to ERA5, all the REMO and ROM fields have been interpolated in the ERA5 mesh, with a regular grid of 0.25°x0.25°, using a distance weighted average remapping of the four nearest neighbors values. Applying the K-G criteria, a climate type for each dataset and each grid cell within the regional domain is obtained. Then, the similarity of their K-G climate types distributions is assessed using the kappa agreement coefficient for categorical scales defined by Cohen (1960), also known as Heidke Skill Score (HSS). A more detailed comparison is performed using the matching matrix method, which is used to compare the climate type assigned to each domain cell using information from two different climate datasets. Matrix elements M(i,j) are the number of cells which are assigned to climate type i according to the first dataset and to climate type j according to the second dataset. Therefore, diagonal elements M(i,i) represent climate type matches according to both datasets, and off-diagonal elements represent climate type "shifts" from one dataset to the other. The matrices allow us to compare two datasets for the same time period, as well as two different time periods for the same model, for example the end of 20th century and the end of 21st century (Gallardo et al., 2013).

3. Results and discussion

3.1. Validation of present-time results

Results from Fig. 1 were generated by applying the K-G classification criteria to the monthly average temperatures and precipitations for the 1976–2005 period taken from the ERA5 dataset (A), REMOH (B) and ROMH (C). The dominant climate type is Cfb on the three maps, covering more than 50% of the domain (see Table 4), including central Europe, Great Britain and Ireland. The Csa type covers large Mediterranean areas, in the southern half of the Iberian Peninsula, southeast France, west Italy, parts of Greece and Turkey and the north of Morocco, Algeria and Tunisia. Csb climate type is present in the northern half of the Iberian Peninsula and parts of Italy, Greece and Turkey. Cfa is found just south of the Alps and in the Danube basin. Dfb appears in East Europe, the Carpathians and some spots in the Pyrenees and the Alps, Dfc in the Alps and some Carpathian spots and ET in the highest areas of the Alps. Semi-arid BSk is found in the southeast of the Iberian Peninsula, north of the Ebro valley, some spots in the Mediterranean islands, southeast of Italy and areas of Morocco, Algeria and Tunisia. Finally, the dry climates BWh and BWk are found mainly in north Africa. In general, the classifications in Fig. 1 compare well to those found in the literature (see e.g., Gallardo et al., 2013; Jylhä et al., 2010; Kottek et al., 2006; Szabó-Takács et al., 2019). For example, according to Fig, 1 of Kottek et al. (2006) we can see that the dominant type in our domain is Cfb, with Dfb areas in eastern Europe, the Carpathians and around the Alps,

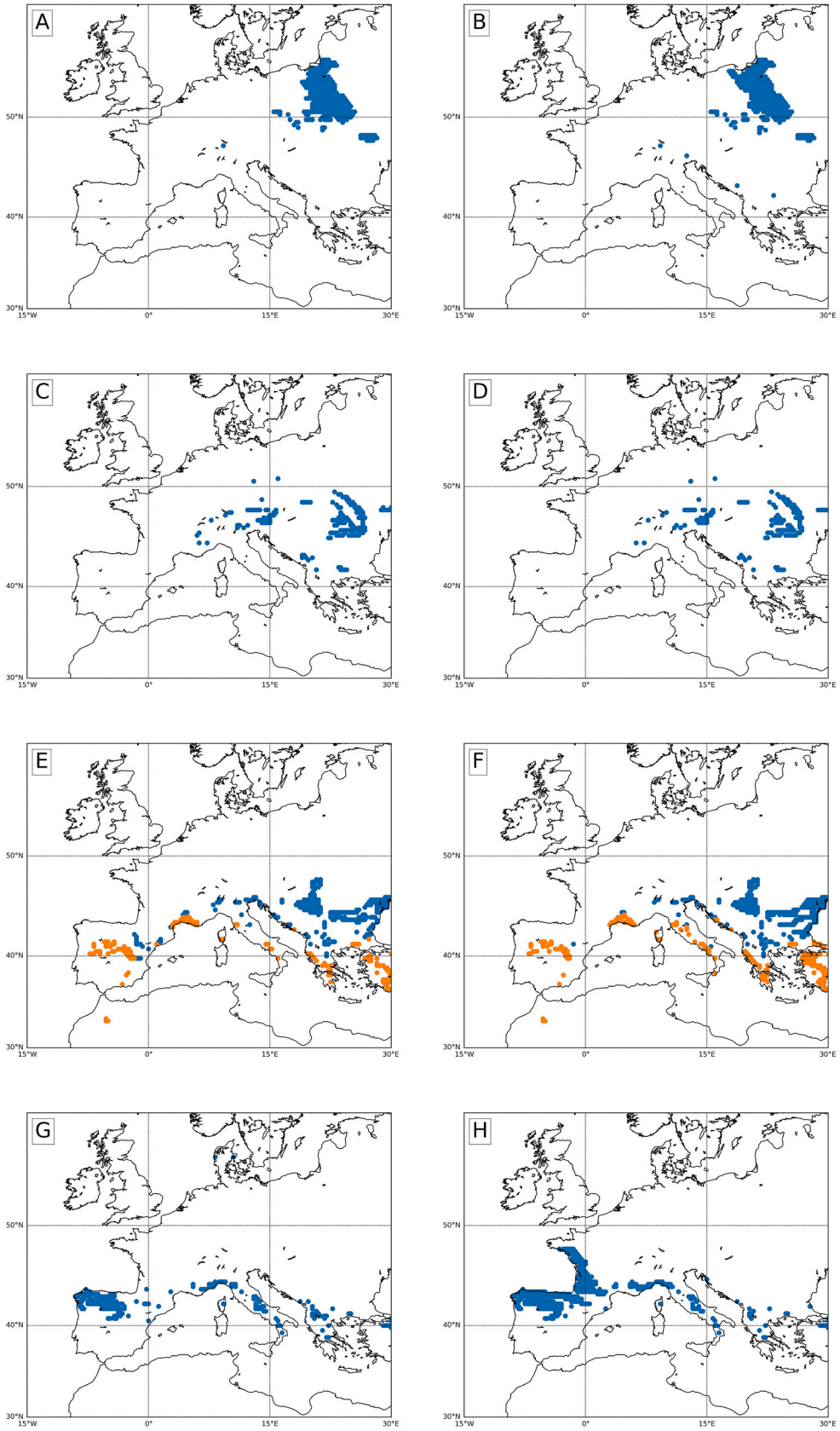

Fig. 3. Maps showing where the K-G classification differs in ERA5 vs REMOH (left column)/ROMH (right column). A, B, Cells classified as Cfb in ERA5 which are classified as Dfb in REMOH/ROMH; C, D, same as A, B for Dfb and Cfb; E, F, same as A,B for Cfa and Cfb in blue dots, and for Csa and Csb in orange dots; G, H, same as A, B for Cfb and Csb. (For interpretation of the references to colour in this figure legend, the reader is referred to the web version of this article.)

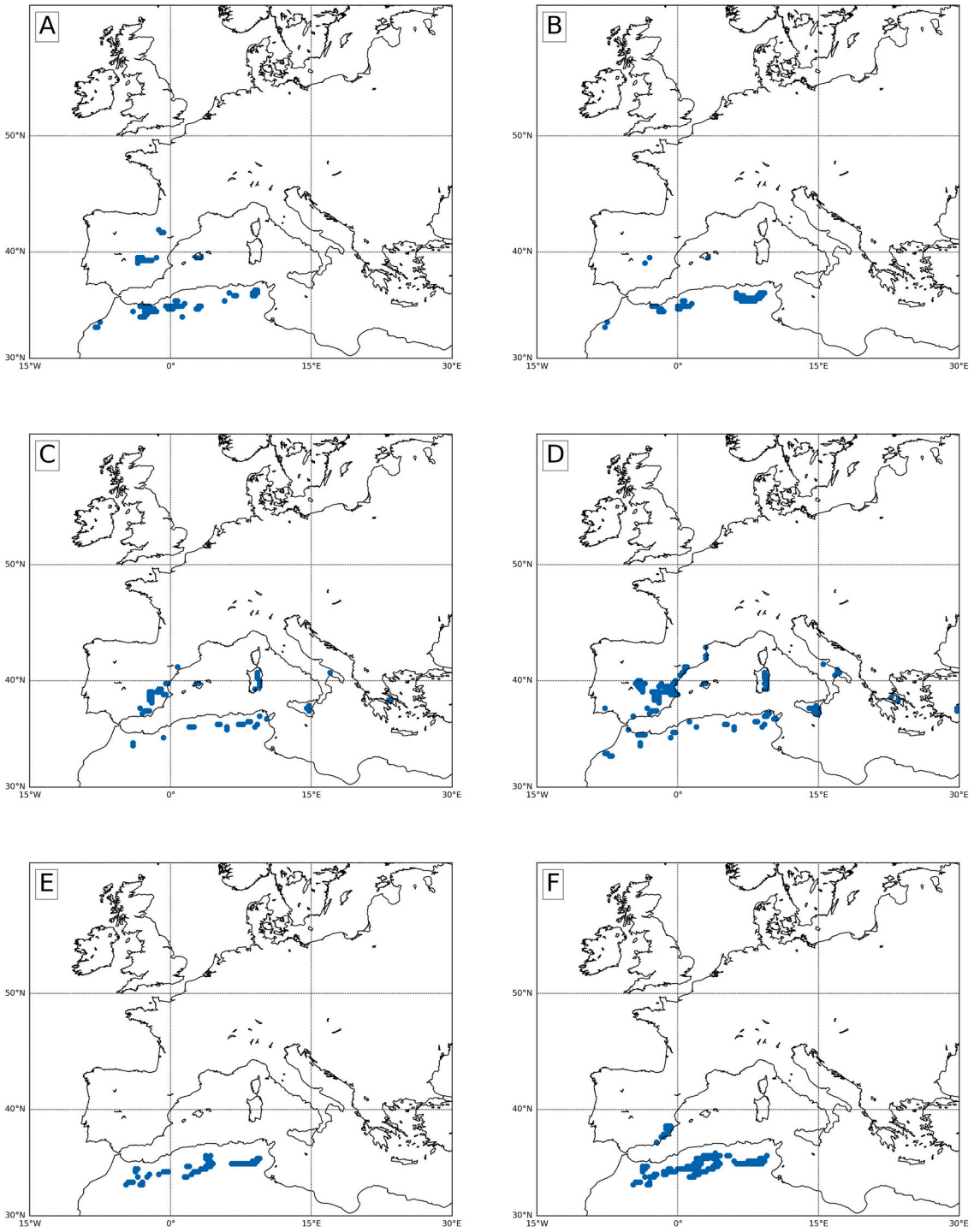

Fig. 4. As in Fig. 3, A, B, Cells classified as BSk in ERA5 which are classified as Csa in REMOH/ROMH; C, D, same as A, B for Csa and BSk; E, F, same as A, B for BSk and BWk.

Csa around the Mediterranean Sea, Csb in the northwest of the Iberian Peninsula, Cfa in the Danube basin and south of the Alps, ET in the highest areas of the Alps, and some BSk spots in the Iberian Peninsula, which is a climate distribution very similar to that depicted in Fig. 1 above. Also Fig. 3a of Jylhä et al. (2010) shows a climate distribution consistent with Fig. 1. Both Kottek et al. (2006) and Jylhä et al. (2010) are based on a slightly earlier period of time.

Analyzing the main differences between the results shown in Fig. 1, Cfa in the Danube basin covers a smaller area in REMOH and ROMH than in the ERA5 reanalysis, where this is substituted by the Cfb type, colder in summer. Also, Cfa does not appear at all in the sub-Pyrenees area in REMOH and ROMH. According to ERA5, Cfb is present in the north of Spain and southwest France, but this is replaced by the drier in summer Csb type in the northwest of Spain in REMOH, and in north Spain and southwest France in ROMH. ROMH reproduces a larger BSk area than ERA5 and REMOH in east Spain, substituting the Csa type, and a small BWk area that is not present with ERA5 and REMOH. Also, the BSk areas to the east of Sardinia, Sicily and the southeast of Italy are larger in ROMH. Regarding cold climates, both REMOH and ROMH simulate a larger ET area in the Alps and smaller Dfb areas in the

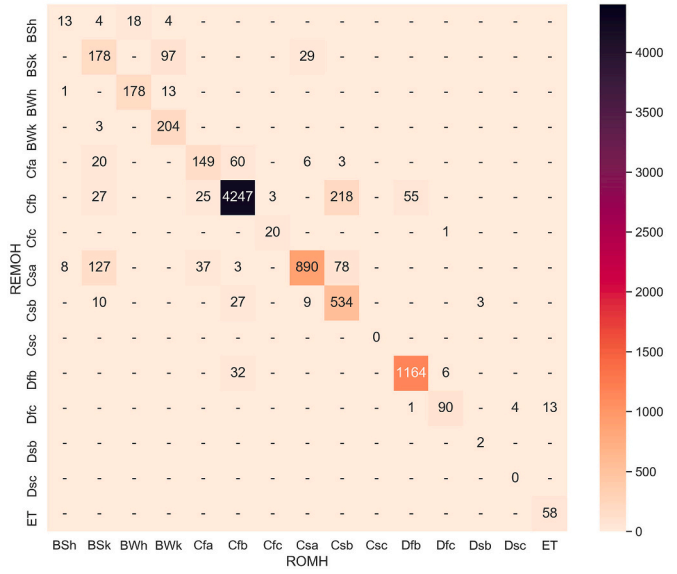

Fig. 5. K-G climate types matching matrix for REMOH and ROMH.

Carpathians in comparison to ERA5. The differences between the panels shown in Fig. 1, which are relatively small, are studied in more detail below and in Section 3.2.

Now we focus on the quantitative comparison between the K-G classification obtained from REMOH/ROMH and that from ERA5. To that end, we compute the kappa agreement coefficient for categorical scales (Cohen, 1960), which was proposed for comparison of vegetation maps (Monserud and Leemans, 1992) and later applied to climate classifications (e.g., Kücken et al., 2009; Tapiador et al., 2019b). The agreement coefficient is a single value ranging between 0 (no agreement) and 1 (perfect agreement). This coefficient corrects the number of matches with the probability of matches by pure chance, allowing for a rank ordering of agreement when comparing categorical maps. Following Tapiador et al. (2019b), we set the threshold for "poor agreement" in coefficient values below 0.5; fair/good agreement [0.5, 0.7]; very good agreement (0.7, 1.0]. Both ROMH and REMOH show good agreement with ERA5 in terms of K-G classification, with an ERA5/REMOH kappa value of 0.70 and a value of 0.64 for ERA5/ROMH. As a reference, the agreement coefficient between ERA5 and *E*-OBS K-G classifications is 0.74.

Next, we focus on the climate type of those cells that do not match the climate type from ERA5. For this quantitative analysis we use matching matrices (also known as confusion or transition matrices in different fields of science). These show in rows the number of cells of the domain for each climate type based on one dataset and in columns the number of domain cells for each climate type based on a second dataset (Gallardo et al., 2013; Lohmann et al., 1993; Tapiador et al., 2019a). Numbers in the diagonal of the matrix represent matches in the corresponding model results and ERA5, while off-diagonal values show non-matches between climate types.

The matching matrices for the REMOH/ROMH comparison against ERA5 are shown in Fig. 2. ERA5 and REMOH K-G types match for 6914cells out of a total of 8672 cells in the domain (80%), while ERA5 and ROMH match in 6538cells (75%). These differences are small considering that we use reanalysis data, on one hand, and downscaled climate data, on the other hand, since they are of the same order of the differences between ERA5 and E-OBS (7147 cells out of 8672 match, or 82%). In Figs. 3 and 4 we represent the locations where the climate types calculated with ERA5 and REMOH or with ERA5 and ROMH do not match. Those cells correspond to the off-diagonal values of Fig. 2 matrices.

Considering the largest off-diagonal values, the main differences between the climate classification from ERA5 and REMOH/ROMH are found in cells classified as Cfb with ERA5. A number of these appear as Dfb with REMOH (361 cells) and ROMH (361 cells). As can be seen in Fig. 3 (A, B), they are located in flat areas to the east of the Vistula (east of Poland and west of Belarus and Ukraine) where the average temperature of the coldest month is lower in REMOH and ROMH. This points to a weaker influence of the Atlantic atmospheric and oceanic circulation on those areas in both simulations. This is consistent with a weakening of the Gulf Stream and North Atlantic currents in both simulations compared to observations, which reduces the heat transport in both oceanic and atmospheric currents towards Europe (Cabos et al., 2020) and results in cold biases in winter on a large surface (see Fig. S.1 of the Supplementary Material). Several empirical studies have pointed to the influence of the Atlantic SST on the variability of the North Atlantic Oscillation (e.g., Czaja and Frankignoul, 2002), but it was Wang et al. (2004) who showed a significant causal relationship between Gulf Stream SST anomalies and the winter NAO pattern. Therefore, a bias in the Gulf Stream SSTs can cause a change in the strength and latitude of the westerly winds that penetrate the European continent to central and eastern Europe in winter and thus change the climate of these regions. Årthun et al. (2018) show how the NAO exerts an influence on the temperatures of these regions.

Also, many cells classified as Dfb with ERA5 appear as Cfb with REMOH (172 cells) and ROMH (149 cells) in areas where the average temperature of the coldest month is warmer according to REMOH/ROMH (Fig. 3C, D). These areas are located around the Carpathians and the Alps.

Fig. 3 (E, F) show in blue dots those cells classified as Cfa with ERA5 which are Cfb with REMOH (250 cells) and ROMH (261 cells). Also, cells classified as Csa with ERA5 which are classified as Csb with REMOH (135 cells) and ROMH (182 cells) are plotted in orange dots. In both cases, the climate types according to REMOH/ROMH correspond to colder summers. For those cells, located in areas below 50°N, in the southern peninsulas, the Balkans and next to the Black Sea, the experiments show a summer cold bias with respect to ERA5 (see Supplementary Material Fig. S.1).

In Fig. 3 (G, H) we observe cells classified as Cfb with ERA5 which appear as Csb with REMOH (201 cells) and ROMH (382 cells) data. Temperate climate with no dry season (similar precipitation in winter and summer) according to ERA5, presents a more humid winter (or relatively a drier summer) in the northwest of the Iberian Peninsula, southwest France and spots in Italy and Greece considering REMOH/ROMH data. This can be seen in winter and summer in Fig. S.2 of the Supplementary Material. In any case, it seems to be an influence of air-sea coupling in ROM, since a comparison of Fig. 3G and H shows how the coupled model extends this change with respect to ERA5 to large areas of the north of the Iberian Peninsula and west of France. The REMOH experiment, forced by MPI-ESM, simulates a strong westerly flow during winter, entering the north of the Iberian Peninsula with a southerly component that increases precipitation compared to ERA5 data in the northwest, while in summer precipitation is small. This causes REMOH to simulate the more unbalanced climate type Csb, instead of the Cfb obtained with ERA5 (Fig. 3G). The coupled model experiment ROMH produces an additional increase of precipitation during winter in the Cantabrian coast and southwest France, extending the area where Csb substitutes the Cfb climate type simulated by ERA5 (Fig. 3H). This points to a different dynamic of the Gulf Stream and North Atlantic Current simulated by MPI-ESM and ROM during winter, that are not able to optimally capture the path of both currents as concluded in Cabos et al. (2020).

According to Keller and Wahl (2021), ERA5 data for Europe shows a humid bias in winter and summer as compared to measurements. This ERA5 bias could be important for the interpretation of the results shown in Fig. 3. However, findings in Fig. 3A through 3F are due to differences in the winter or summer temperatures and findings in Fig. 3G-3H are due to a different winter-summer precipitation distribution. Therefore, none

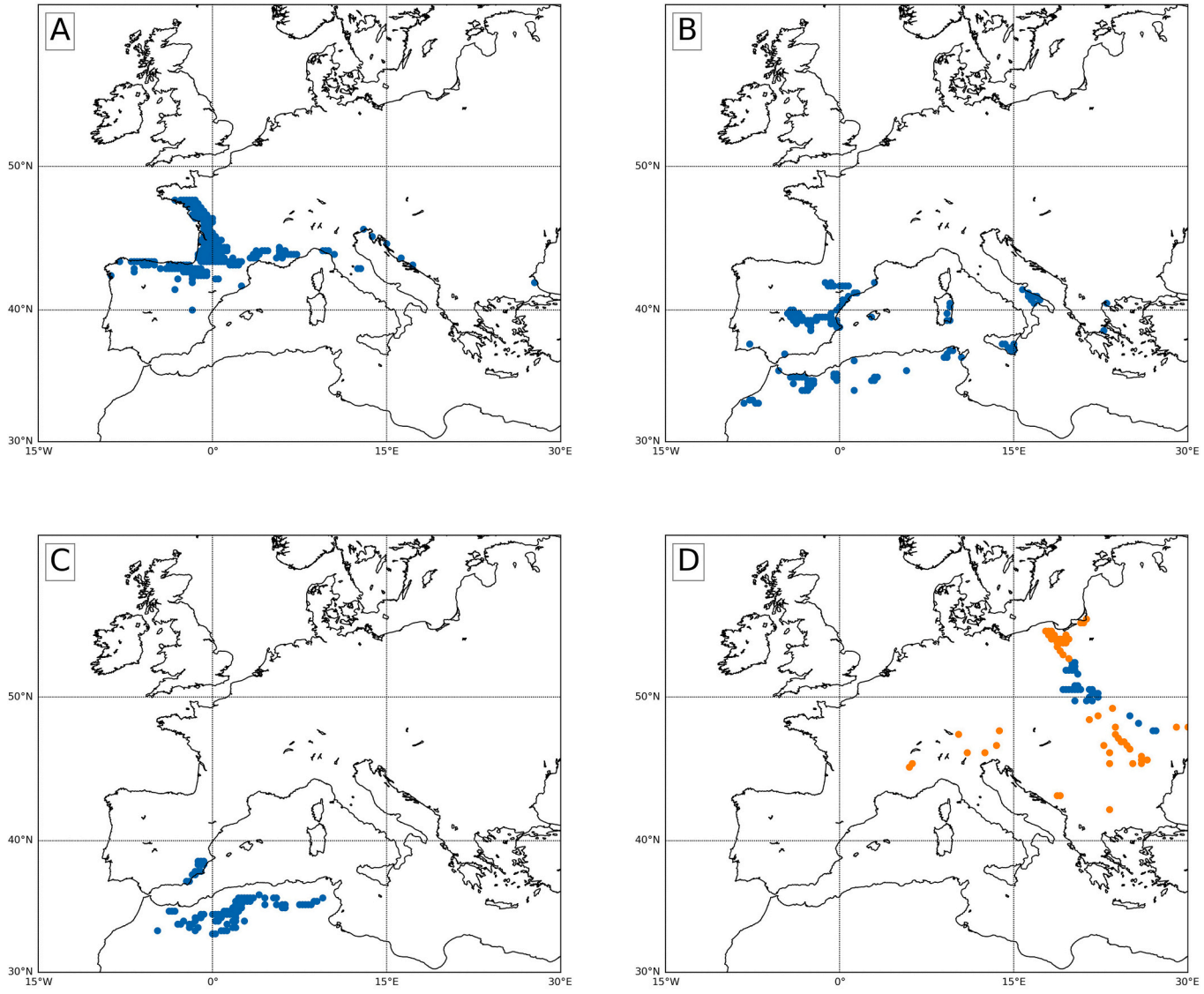

Fig. 6. Locations where the K-G classification differs in REMOH and ROMH. A, cells classified as Cfb in REMOH but as Csb in ROMH; B, same as A for Csa and BSk; C, same as A for BSk and BWk; D, same as A for Dfb and Cfb plotted in blue dots (vice versa for 40 cells also plotted in orange dots). (For interpretation of the references to colour in this figure legend, the reader is referred to the web version of this article.)

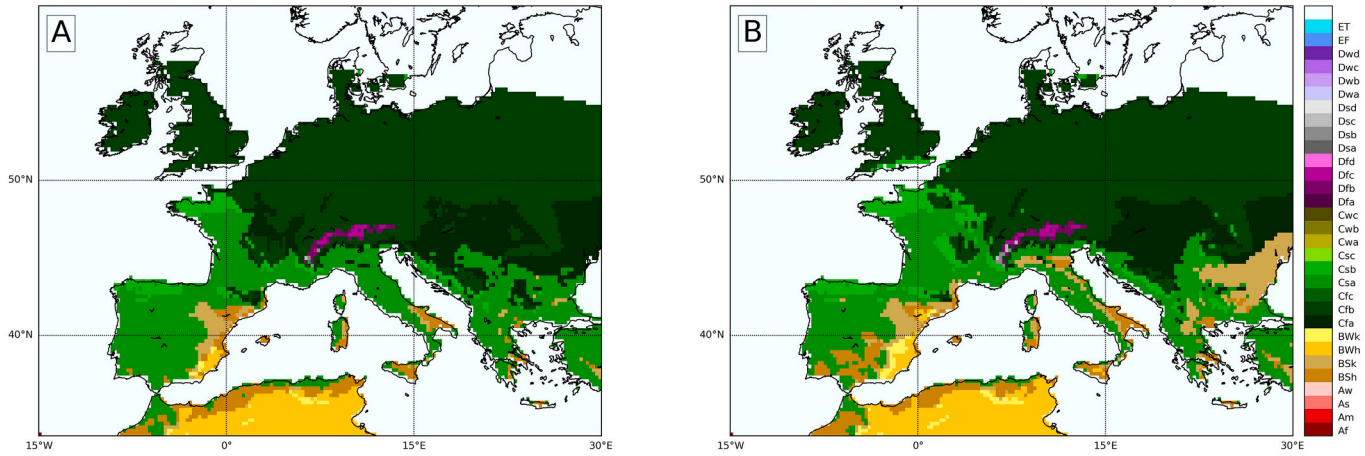

Fig. 7. Köppen-Geiger classification for 2070–2099; A REMO85; B ROM85.

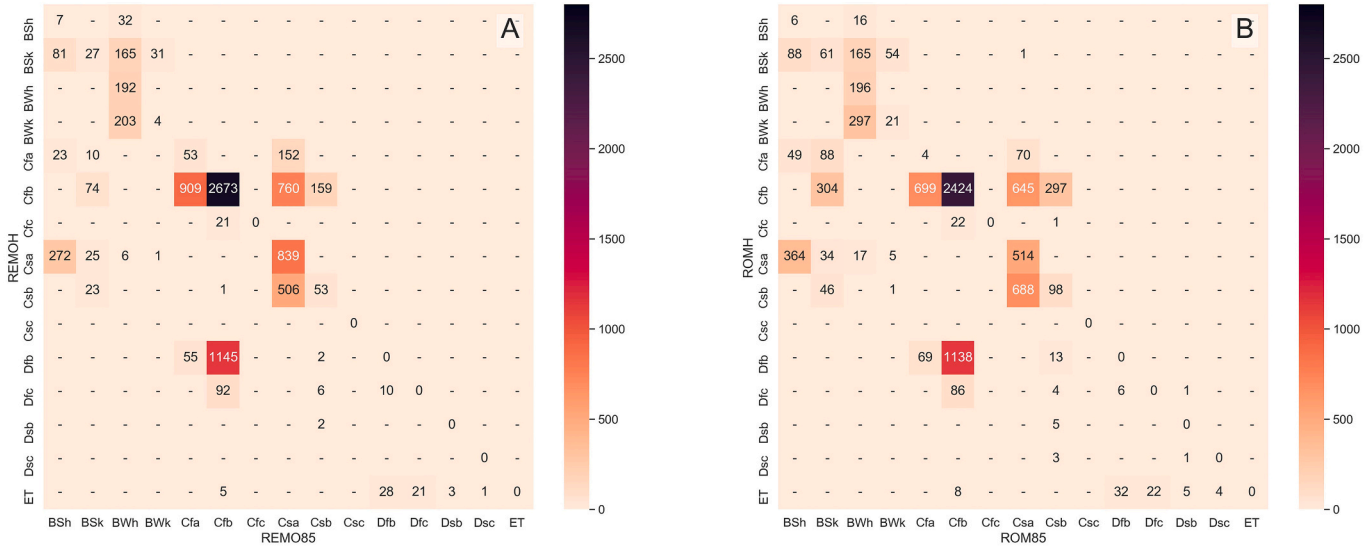

Fig. 8. Climate types matching matrix. a, REMOH vs REMO85; b, ROMH vs ROM85.

of them can be attributed to the ERA5 wet bias in winter and summer noticed in Keller and Wahl (2021).

Domain cells classified as semi-arid climate BSk with ERA5 which appear as more humid Csa with REMOH (72 cells) and ROMH (53 cells) are depicted in Fig. 4 (A, B), corresponding to central Spain and the African coast of the Alboran Sea (west Mediterranean). On the contrary, cells classified as Csa with ERA5 which are classified as BSk with REMOH (59 cells) and ROMH (128 cells) can be seen in Fig. 4 (C, D), also in spots of Mediterranean coasts. The shifts between these two climate types are caused by total annual precipitation differences in Western Mediterranean areas. Mediterranean climates are usually so close to semi-arid conditions that slight underestimations of rainfall in a few years cause the climate to fall from Csa to BSk.

Finally, Fig. 4 (E, F) depicts cells classified as semi-arid BSk with ERA5 that appear as desert type BWk according to REMOH (56 cells) and ROMH (126 cells) due to smaller annual precipitations simulated by REMOH/ROMH. According to REMOH, this only occurs in areas of north Africa, while with ROMH it happens mainly in regions of north Africa, but also in a few spots to the southeast of Spain.

Again, for the interpretation of the results shown in Fig. 4 we have to consider that according to Keller and Wahl (2021) ERA5 data for Europe shows a humid bias in winter and summer as compared to measurements. Therefore, in general one can expect climate types to be more humid when simulated with ERA5 data than the actual climates over Europe. This is consistent with the differences shown in Fig. 4C-4D and Fig. 4E-4F, where regions with climate types Csa and BSk in ERA5, have the drier types BSk and BWk according to REMOH/ROMH. Therefore, instead of a slight precipitation underestimation by REMOH/ROMH, this result could be attributed to an overestimation by ERA5, or to a combination of both factors. However, the results shown in Fig. 4A-4B would be consistent with a humid bias in the REMOH/ROMH data and thus it cannot be attributed to the ERA5 humid bias.

In sum, the validation of REMOH and ROMH shows that the models are able to reproduce the climate types generated in the reanalysis in most of the domain. In fact, the comparison of ERA5 and a European daily high-resolution gridded dataset, such as E-OBS (not shown), in terms of K-G types results in a similar agreement (7147 out of 8672 domain cells, or 82%) with a kappa coefficient of 0.74. This shows that the REMOH/ROMH experiments are as close to ERA5 in terms of K-G classification as other observational datasets.

In winter, REMOH and ROMH present a cold bias compared to ERA5 in areas of northeast Europe caused by a weaker influence of the model Gulf Stream, through the North Atlantic Oscillation, in MPI-ESM (which is used to force REMO) and ROM, and a warm bias around the Carpathians and the Alps possibly due to differences in the orography of the model. REMOH and ROMH also show a generalized summer cold bias in areas below 50°N and a summer dry bias in west Mediterranean areas. The ocean-atmosphere coupling in ROM results in drier climates in several areas of the Iberian Peninsula.

3.2. Comparison of REMO and ROM present-time results

As stated above, maps in Fig. 1 (B, C) were generated by applying the K-G classification criteria to the monthly average temperatures and precipitations from REMOH and ROMH. The agreement coefficient between them is 0.84 (very good agreement) with a climate type match in 7727 out of 8672 (89%), pointing to a small difference between the models. The matching matrix for these two experiments is shown in Fig. 5.

In the largest off-diagonal value 218 cells classified as Cfb in REMOH appear as Csb in ROMH (27 vice-versa not plotted). The locations where this occurs are shown in Fig. 6A, mainly covering areas of the north of Spain, west and south of France. The difference between Csb and Cfb points to a more balanced yearly precipitation estimated by REMOH, with drier (wetter) summers (winters) estimated by ROMH. This is consistent with Fig. 15-C and 15-D of Cabos et al. (2020) calculated for the same period. The average precipitation difference between ROMH and REMOH is included in the Supplementary Material as Fig. S.3. In that figure, and more clearly in Fig. 15C of Cabos et al. (2020), we observe a wet bias in winter in south France and the Cantabrian coast and a dry bias in winter in the Iberian Peninsula and some locations of the Mediterranean basin in ROM. Also, a generalized dry bias can be identified over the aforementioned areas in summer.

Next highest off-diagonal value corresponds to 127 cells classified as Csa with REMOH, which are BSk (cold steppe), according to ROMH. These locations are shown in Fig. 6B and correspond to areas of central and east Spain, southeast Italy, south of Sicily, east of Sardinia and some points in north Africa. Higher total annual precipitation in REMOH (lower in ROMH) is consistent with Fig. 15C and 15D of (Cabos et al., 2020). In Supplementary Material Fig. S.3 a dry bias is identified in ROMH across the Mediterranean Sea areas. 97 cells are classified as BSk with REMOH and are BWk (cold desert) according to ROMH. Locations are shown in Fig. 6C. Although most are out of Europe, some of them are in the southeast of Spain. The shift from BSk to BWk points to an even drier climate in ROMH, consistent with what has been stated above. 32 cells classified as Dfb in REMOH appear as Cfb in ROMH, plotted with

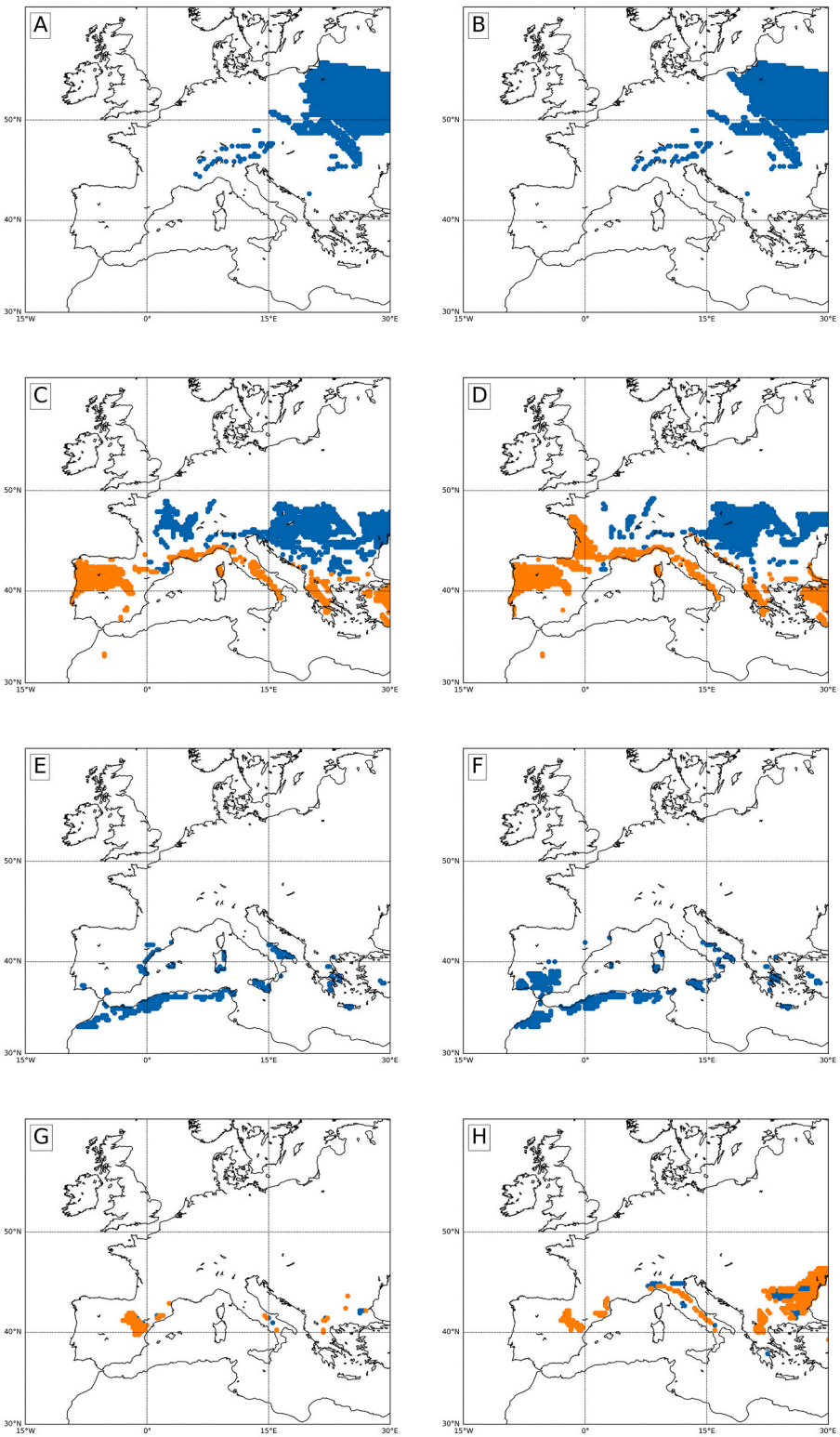

Fig. 9. Maps showing where K-G climate types change by the end of the 21st century, comparing REMOH vs REMO85 (left column) and ROMH vs ROM85 (right column). A, B, cells classified as Dfb in REMOH/ROMH which are classified as Cfb in REMO85/ROM85; C, D, same as A, B for Cfb/Csb shift to Cfa/Csa. Cfb-Cfa transition plotted in blue, Csb-Csa in orange; E, F, same as A, B for Csa shift to BSh; G, H, same as A, B for Cfa (blue) and Cfb (orange) shift to BSk. (For interpretation of the references to colour in this figure legend, the reader is referred to the web version of this article.)

blue dots in Fig. 6D (vice versa for 55 cells also plotted in orange dots). A small difference in temperature in the coldest month can drive a change of this type in K-G climate type classification. This could be related to a different dynamic of the atmosphere at the entrance to the European continent of air masses from the Atlantic Ocean in plain areas of east Europe and a different temperature behavior with altitude in REMOH and ROMH in a few spots around the Alps and the Carpathians.

We can conclude that most differences between both experiments in terms of climate types can be explained by different precipitation regimes, basically due to a dry (wet) bias of ROMH during summer (winter) in some areas, and a year-round dry bias of ROMH in other areas, when compared to REMOH. Supplementary material Fig. S.3 presents the differences between REMOH and ROMH in summer and winter precipitation. Fig. S3.b shows that ROMH simulates a drier

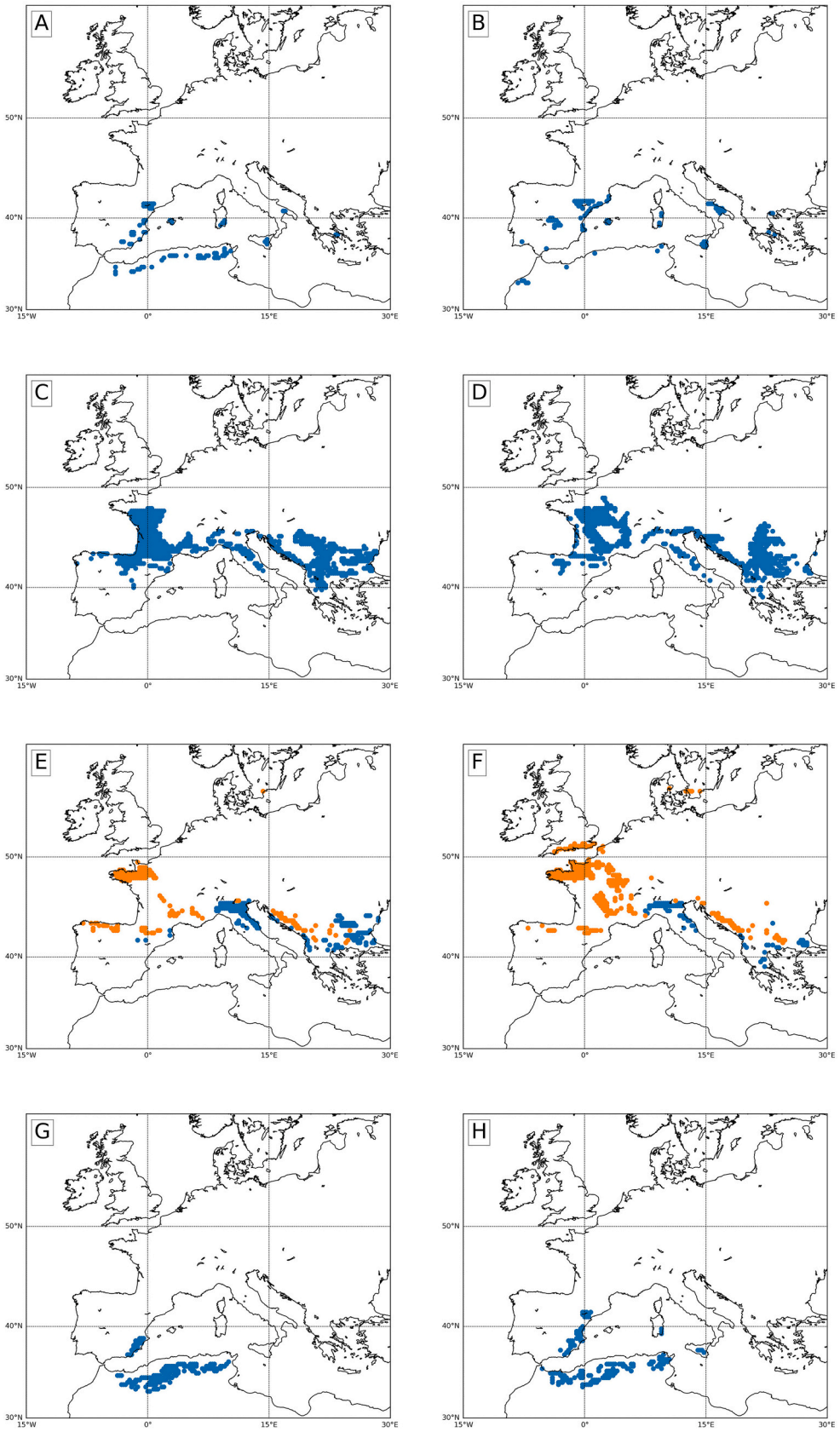

Fig. 10. As in Fig. 9, A, B, BSk shift to BSh; C, D, Cfb shift to Csa; E, F, Cfa/Cfb shift to Csa/Csb. Cfa to Csa transition plotted in blue, Cfb to Csb in orange; G, H, BSk shift to BWh. (For interpretation of the references to colour in this figure legend, the reader is referred to the web version of this article.)

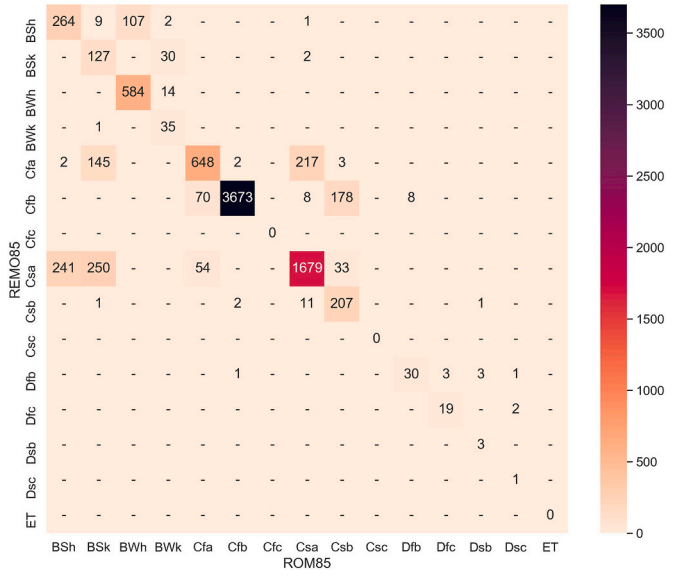

Fig. 11. End of the 21st century comparison between REMO85 and ROM85 K-G classification.

summer in most of Europe, with exceptions in the Alps and the Danube basin. However, as shown in Fig. S3.a, during winter this is only true for the Mediterranean basin, while more precipitation is simulated by ROMH north of the Pyrenees and the Alps. Additional differences may be due to a different dynamic of air masses entering from the Atlantic Ocean.

3.3. *REMO and ROM future-climate experiments for the RCP8.5 scenario*

To analyze the climate change signal, we select the RCP8.5 scenario to maximize it, and therefore to enhance the effect of ocean-atmosphere coupling. We then apply the K-G classification criteria to REMO85 and ROM85 (2070–2099). Results are shown in Fig. 7.

Comparing, in terms of K-G types distribution, REMOH (1976–2005) to REMO85 (2070–2099), the agreement coefficient gives a value of 0.23, while the same comparison between ROMH and ROM85 yields an agreement coefficient of 0.18. The poor agreement of the end of 21st century RCP8.5 scenario climate types (Fig. 7A and B) with the present-time simulations (Fig. 1B and C) indicates a relevant change in climate types, especially in the ROM experiments, where air-sea interactions are active. The general trends in surface temperature and precipitation for winter and summer can be seen in Fig. 3(D, H) and Fig. 4(D, H) of Sein et al. (2020), which show a year-round warming, a precipitation increase in winter and precipitation decrease in summer in our area of study. These end of century trends explain the area reduction of cold climate types (Dfb, ET), as well as the area expansion of hot summer climate types (Cfa, Csa) and hot arid types (BWh, BSh) observed in Fig. 7.

Using the matching matrix method to compare REMOH to REMO85 and ROMH to ROM85 (Fig. 8), we note that in REMO85 only 3848 cells (44%) and in ROM85 only 3324 cells (38%), out of a total of 8672 cells in the domain, maintain their present-time K-G climate type at the end of the 21st century. Climate Dfb disappears in the RCP8.5 scenario, except in the Alps, becoming Cfb, with warmer winters, in those regions shown in Fig. 9 (A, B), which include east Europe, the Carpathians and the Alps. ET (tundra) climate, found in the Alps at the present time, completely disappears in the future. These trends for central Europe, near the Alps, can be found in Skalák et al. (2018), Figs. 2-3, for a similar scenario (IPCC SRES A1B emission scenario) with Dfb and Cfb climates shifting to Cfb and Cfa, and ET disappearing. Many areas below 50°N with Cfb climate shift to Cfa and most areas with Csb climate shift to Csa (summer becomes hotter in both cases) in the RCP8.5 scenario, as can be seen in Fig. 9 (C, D), consistently with Fig. 3h of (Sein et al., 2020), where those areas suffer a more intense warming. Areas of the African Mediterranean coast, Spain, Sardinia and Sicily, south Italy, and Greece Aegean coast shift from a temperate Csa climate with hot/dry summer to an even drier BSh climate, Fig. 9 (E, F). Areas in northeast Spain, Italy, Romania (Black Sea) and north Greece with fully humid temperate climates Cfa and Cfb shift to dry BSk as shown in Fig. 9 (G, H). Dry BSk regions in Spain and south Italy become hotter BSh, Fig. 10 (A, B). A shift from Cfb to Csa due to hotter and drier summers (relatively to more humid winters) is depicted in Fig. 10 (C, D), covering parts of west France, north Spain and Italy, Adriatic coast and the Balkans. Year-round precipitation is more unbalanced (summers are drier or winters are more humid) in the areas where climate type shifts from Cfa to Csa and from Cfb to Csb, Fig. 10 (E, F). Finally, a great portion of BSk areas shift to BWh, see Fig. 10 (G, H). This means that they become hotter and more arid.

Comparing the trends in K-G types shifts by the end of the 21st century to those found in other works, we see that for the Iberian Peninsula they are consistent with (B, D) of (Andrade and Contente, 2020): the Cfb area in the Pyrenees almost disappears, the BSk type areas enlarge, and some BSh/BWh hot arid areas appear on the southeast coast of the Iberian Peninsula. Also, for a similar emissions scenario (IPCC SRES A1B emission scenario), the same trends for central Europe are found in Skalák et al. (2018) Figs. 2-3 and for Europe in Jylhä et al. (2010) Fig. 3d. In Fig. 3 of a global analysis using the Köppen-Trewartha climate classification by Belda et al. (2016), similar trends are found. The local climate shift in the Alps, where ET disappears and is substituted by Dfb and Cfb has also been reported in Rubel et al. (2017) (lower panel of Fig. 2). In general, the climate change signal obtained with REMO85 and ROM85 is very similar. Focusing on the differences between them, ROM85 simulates a transition to semi-arid climate BSk in a large region west of the Black Sea and along Italy, not found in REMO85 (Fig. 9G and H). This aridification signal confirms findings from Jylhä et al. (2010) in this same region. Also, ROM85 shows a dry BSh area to the south of the Iberian Peninsula which is not simulated in REMO85 (Fig. 9E and F).

To allow for a quantification of the changes presented above, we include in Table 4 the number of cells (and its percentage) covered by each climate type in the different datasets. Each cell corresponds to an approximate area of 780 km^2 (a square of approximately 28 km side).

Focusing on the largest area changes simulated with REMO, we observe in Table 4 that comparing REMOH (1976–2005) to REMO85 (2070–2099) climate Dfb decreases from 13.9% of the domain area to 0.4%, practically disappearing at the end of 21st century. Cfb initially represents 52.8% of the area, decreasing to 45.4%. Csb reduces from 6.7% to 2.6%. Also, Csa climate type covers 13.2% initially and increases to 26.0%, Cfa extends from 2.7% to 11.7%, BWh from 2.2% to 6.9% and BSh from 0.4% to 4.4%.

Comparing the areas covered in ROMH (1976–2005) to those found with ROM85 (2070–2099) the area covered by the Dfb climate decreases from 14.1% to 0.4% of the domain. Cfb goes from an area of 50.4% to 42.4%, and Csb decreases from 9.6% to 4.9%. In the opposite direction, Csa goes from 10.8% to 22.1%, Cfa from 2.4% to 8.9%, BWh from 2.3% to 8.0%, and BSh from 0.3% to 5.8%.

Although results presented in this section are based on two simulations, the climate distributions under RCP8.5 are consistent with those found in previous works (Andrade and Contente (2020) for the Iberian Peninsula, Skalák et al. (2018) for Central Europe, Belda et al. (2016) and Jylhä et al. (2010) for Europe, Rubel et al. (2017) for the Alps), as discussed above. Also interestingly, our setup allows us to consider simultaneously the Mediterranean and North Atlantic Ocean, which are both important for the European climate. Whilst it would be interesting to have performed this work with a model ensemble, such a set of regional climate coupled and uncoupled simulations is not available to date. For example, in the EuroCORDEX initiative (Jacob et al., 2020) no atmosphere-ocean coupled models are used and, in addition to that, the

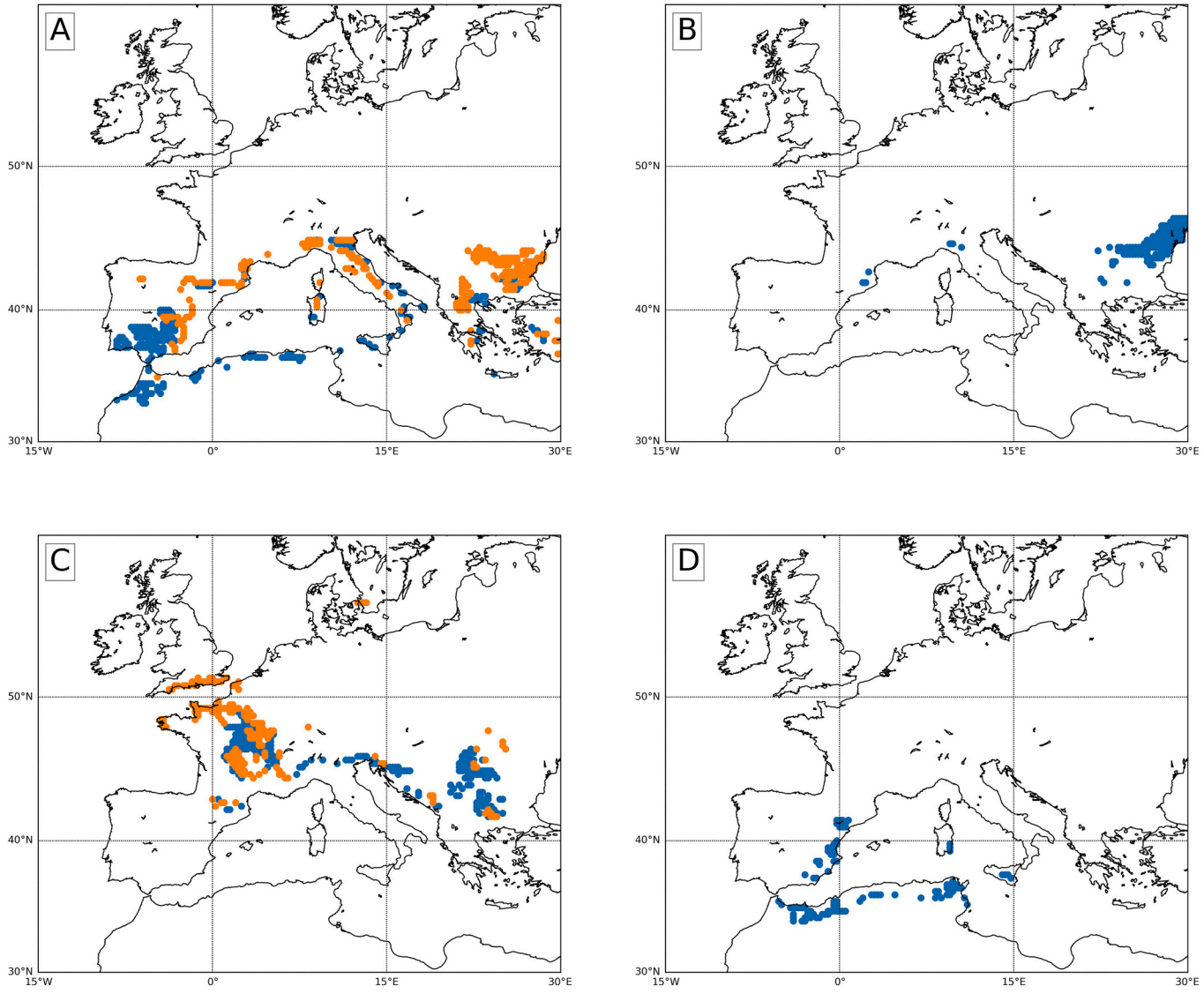

Fig. 12. Locations where the K-G classification differs in REMO85 and ROM85. A, cells classified as Csa in REMO85 which are classified as BSh (blue dots)/BSk (orange dots) with ROM85; B, same as A for Cfa and BSk; C, same as A for Cfa and Csa in blue dots, orange dots for the Cfb to Csb mismatch; D, same as A for BSh and BWh. (For interpretation of the references to colour in this figure legend, the reader is referred to the web version of this article.)

domain does not include completely the western North Atlantic.

3.4. REMO and ROM differences in future climate

Now we focus on the differences between the REMO85 and ROM85 projections for the end of the 21st century (2070–2099) to assess the effect of air-sea coupling itself. To that end, we compare the K-G types maps from Fig. 7 (A, B). Both models show a very good agreement, with a kappa coefficient of 0.78. Also, 7270 cells out of 8672 (84% of the domain) are assigned the same climate type. The corresponding matching matrix is shown in Fig. 11. A detailed analysis of the off-diagonal values shows that the main differences are:

- Csa type areas in REMO85 that are classified as BSk (250 cells) or BSh (241) with ROM85. These regions are found in southern latitudes near the Mediterranean Sea (Fig. 12A).
- A region next to the Black Sea with Cfa climate in REMO85 is assigned to BSk in ROM85 (145 cells). It is plotted in Fig. 12B.
- Fig. 12C shows in blue dots the locations of Cfa type in REMO85 which are Csa in ROM85 (217 cells) and in orange dots those which are Cfb in REMO85 and Csb in ROM85.
- Some zones of the Western Mediterranean coasts are classified as BSh in REMO85 but as BWh in ROM85. They are shown in Fig. 12D.

All these mismatches correspond to drier climate types, or climate types with less balanced winter-summer precipitation distribution, estimated with ROM85. In Fig. 15E and 15F of de la Vara et al. (2021), also included in the Supplementary Material as Fig. S.4, the dry bias of the ROM85 projection with respect to the REMO85 one in many parts of southern Europe during winter and some parts of northern Europe during summer is depicted. In de la Vara et al. (2021) it is described how the North Atlantic precipitation in ROM85 is smaller than in REMO85 (forced by MPI-ESM) because sea-surface temperature is lower due to the air-sea coupling, which reduces the latent heat flux into the atmosphere, and thus water vapor content and precipitation. A similar mechanism is proposed for the Western Mediterranean Sea in de la Vara et al. (2021) affecting the Iberian Peninsula. Fig. 12E and F of de la Vara et al. (2021) show the sea surface temperature difference between

ROM85 and REMO85 around the European coasts, where a cold bias in ROM85 is noticed especially during summer (Fig. S.5 of the Supplementary Material). Therefore, ROM85 would simulate drier conditions, as compared to REMO85, in large areas of Southern Europe due to the influence of colder water in the North Atlantic Ocean and Mediterranean Sea. This mechanism has been proposed by de la Vara et al. (2021) for the Iberian Peninsula and the Western Mediterranean and can be assumed to be active in the Eastern Mediterranean too. de la Vara et al. (2021) also cautions that the relationship between the latent heat fluxes simulated by ROM and REMO has a strong dependence on the season and the region, being clearly different in the Atlantic than in the Mediterranean.

4. Conclusions

In this work we use the Köppen-Geiger climate types classification to study the impact of air-sea coupling on the simulation of present and future climate by the end of the 21st century in the European region. To that end we use data from a set of present-time (1976–2005) and future-time (2070–2099) climate simulations performed under the RCP8.5 scenario with the regionally air-sea coupled model ROM and its atmospheric component REMO. The domain includes explicitly the North Atlantic, the Mediterranean Sea and the Black Sea. This is relevant since the European climate is subjected to their influence. This approach provides a novel insight into the impact of air-ocean coupling on the representation of the European climate. The most relevant findings from this work can be summarized as follows.

Present-time climate (1976–2005)

- In terms of K-G types both REMO and ROM show very similar distributions with ERA5. A comparison of two observational datasets, ERA5 and *E*-OBS, reveals differences of the same order.
- REMO and ROM show colder climates in summer in southern areas and colder climates in northeast Europe in winter, while around the Alps and the Carpathians the simulated climate types are warmer in the two seasons. The colder climate types could be related to a smaller influence of the Atlantic in Europe due to a weaker than in observations Gulf Stream and north Atlantic current. Those currents indirectly affect northeast Europe through the North Atlantic Oscillation.
- REMO and ROM show drier climates in some western Mediterranean areas and climates with more humid winters (relatively drier summers) in north Spain and southwest France.
- We find minor differences between K-G climate types distribution in REMO and ROM. These are mainly caused by different precipitation regimes, due to a wet (dry) bias of ROM during winter (summer) in some areas, and a year-round dry bias of ROM when compared to REMO in other areas. REMO and ROM experiments also shift from Dfb to Cfb and vice versa in a few locations, due to differences in the temperature of the coldest month.

Future-time climate (2070–2099)

- Under the RCP8.5 scenario the K-G type changes in 55% and 61% of the area of study for REMO and ROM, respectively.
- Discrepancies between REMO and ROM RCP8.5 experiments in terms of K-G types distribution are small. By the end of the 21st century both models project a reduction of regions with cold climate types (the Tundra type disappears in the domain) and an expansion of areas with hot summers and hot arid climate types.
- ROM tends to simulate slightly drier climates than REMO at the end of the 21st century in areas depicted in Fig. 12 due to the influence of colder than in the driving model sea surface temperatures in the North Atlantic Ocean and Mediterranean Sea.

Recent comparisons of CMIP5 and CMIP6 experiments (e.g., Hamed et al., 2021) suggest that an extension of this work using CMIP6 results would benefit from a higher reliability and a reduced uncertainty of climate projections. Also, this work could be extended in the future using an ensemble of regional models instead of a single model. However, up to date there are not many models with the characteristics of ours, and constructing an ensemble would be very difficult. An alternative would be to compare directly to climates from a EURO-CORDEX ensemble, although that ensemble would not include the effect of ocean-atmosphere coupling since EURO-CORDEX models are not coupled, and the domain would not completely include the North Atlantic Ocean. A third line of extension of our work would be a sensitivity analysis to the initial conditions, which could help to establish more firmly some of the conclusions presented. We anticipate that the impact of ocean-atmosphere coupling in regional models could be important for the analysis and projection of climate types in other regions of the world.

CRediT authorship contribution statement

Rafael Falquina: Methodology, Software, Formal analysis, Writing – original draft, Visualization. **Alba de la Vara:** Conceptualization, Writing – review & editing. **William Cabos:** Writing – review & editing, Resources. **Dmitry Sein:** Data curation. **Clemente Gallardo:** Conceptualization, Supervision, Writing – review & editing.

Declaration of Competing Interest

The authors declare that they have no known competing financial interests or personal relationships that could have appeared to influence the work reported in this paper.

Acknowledgements

We acknowledge Copernicus, which provides ERA5. Monthly averaged data on single levels from 1979 to present were downloaded from the Copernicus Climate Change Service (C3S) Climate Data Store. The results contain modified Copernicus Climate Change Service information 2021. Neither the European Commission nor ECMWF is responsible for any use that may be made of the Copernicus information or data it contains.

We acknowledge the World Climate Research Programme's Working Group on Coupled Modelling, which is responsible for CMIP, and we thank the MPI-ESM group for producing and making available their model output. For CMIP the U.S. Department of Energy's Program for Climate Model Diagnosis and Intercomparison provides coordinating support and led development of software infrastructure in partnership with the Global Organization for Earth System Science Portals.

Alba de la Vara has been partially funded by the Spanish Ministry of Science, Innovation and Universities, the Spanish State Research Agency and the European Regional Development Fund, through grant CGL2017-89583-R. William Cabos has been funded by the Alcala University project PIUAH21/CC-058.

Appendix A. Supplementary data

Supplementary data to this article can be found online at https://doi.org/10.1016/j.atmosres.2022.106223.

References

Allam, A., Moussa, R., Najem, W., Bocquillon, C., 2020. Specific climate classification for Mediterranean hydrology and future evolution under Med-CORDEX regional climate model scenarios. Hydrol. Earth Syst. Sci. 24, 4503–4521. https://doi.org/10.5194/hess-24-4503-2020.

Andrade, C., Contente, J., 2020. Köppen's climate classification projections for the Iberian Peninsula. Clim. Res. 81, 71–89.

Årthun, M., Kolstad, E.W., Eldevik, T., Keenlyside, N.S., 2018. Time scales and sources of European temperature variability. Geophys. Res. Lett. 45, 3597–3604. https://doi.org/10.1002/2018GL077401.

Barredo, J.I., Mauri, A., Caudullo, G., 2020. Alpine tundra contraction under future warming scenarios in Europe. Atmosphere (Basel) 11. https://doi.org/10.3390/atmos11070698.

Beck, H.E., Zimmermann, N.E., McVicar, T.R., Vergopolan, N., Berg, A., Wood, E.F., 2018. Present and future köppen-geiger climate classification maps at 1-km resolution. Sci. Data 5, 1–12. https://doi.org/10.1038/sdata.2018.214.

Belda, M., Holtanová, E., Kalvová, J., Halenka, T., 2016. Global warming-induced changes in climate zones based on CMIP5 projections. Clim. Res. 71, 17–31. https://doi.org/10.3354/cr01418.

Borchert, J.R., 1953. Regional differences in the world atmospheric circulation. Ann. Assoc. Am. Geogr. 43, 14–26.

Cabos, W., Sein, D.V., Pinto, J.G., Fink, A.H., Koldunov, N.V., Alvarez, F., Izquierdo, A., Keenlyside, N., Jacob, D., 2017. The South Atlantic Anticyclone as a key player for the representation of the tropical Atlantic climate in coupled climate models. Clim. Dyn. 48, 4051–4069. https://doi.org/10.1007/s00382-016-3319-9.

Cabos, W., Sein, D.V., Durán-Quesada, A., Liguori, G., Koldunov, N.V., Martínez-López, B., Alvarez, F., Sieck, K., Limareva, N., Pinto, J.G., 2019. Dynamical downscaling of historical climate over CORDEX Central America domain with a regionally coupled atmosphere–ocean model. Clim. Dyn. 52, 4305–4328. https://doi.org/10.1007/s00382-018-4381-2.

Cabos, W., de la Vara, A., Álvarez-García, F.J., Sánchez, E., Sieck, K., Pérez-Sanz, J.I., Limareva, N., Sein, D.V., 2020. Impact of ocean-atmosphere coupling on regional climate: the Iberian Peninsula case. Clim. Dyn. 54, 4441–4467. https://doi.org/10.1007/s00382-020-05238-x.

Castro, C.L., Pielke, R.A., Leoncini, G., 2005. Dynamical downscaling: Assessment of value retained and added using the Regional Atmopsheric Modeling System (RAMS). J. Geophys. Res. D Atmos. 110, 1–21. https://doi.org/10.1029/2004JD004721.

Chen, D., Chen, H.W., 2013. Using the Köppen classification to quantify climate variation and change: an example for 1901-2010. Environ. Dev. 6, 69–79. https://doi.org/10.1016/j.envdev.2013.03.007.

Cohen, J.A., 1960. A coefficient of agreement for nominal scales. Educ. Psychol. Meas. XX 37–46.

Czaja, A., Frankignoul, C., 2002. Observed impact of Atlantic SST anomalies on the North Atlantic Oscillation. J. Clim. 15, 606–623.

Darmaraki, S., Somot, S., Sevault, F., et al., 2019. Future evolution of marine heatwaves in the Mediterranean Sea. Clim. Dyn. 53 (3), 1371–1392. https://doi.org/10.1007/s00382-019-04661-z Future.

Davies, H., 1976. A lateral boundary formulation for multi-level prediction models. Q. J. R. Meteorol. Soc. 102, 405–418.

de la Vara, A., Cabos, W., Sein, D.V., Teichmann, C., Jacob, D., 2021. Impact of air–sea coupling on the climate change signal over the Iberian Peninsula. Clim. Dyn. https://doi.org/10.1007/s00382-021-05812-x.

Domínguez, M., Romera, R., Sánchez, E., Fita, L., Fernández, J., Jiménez-Guerrero, P., Montávez, J.P., Cabos, W.D., Liguori, G., Gaertner, M.Á., 2013. Present-climate precipitation and temperature extremes over Spain from a set of high resolution RCMs. Clim. Res. 58, 149–164. https://doi.org/10.3354/cr01186.

Dubreuil, V., Fante, K.P., Planchon, O., Sant'Anna Neto, J.L., 2019. Climate change evidence in Brazil from Köppen's climate annual types frequency. Int. J. Climatol. 39, 1446–1456. https://doi.org/10.1002/joc.5893.

Falquina, R., Gallardo, C., 2017. Development and application of a technique for projecting novel and disappearing climates using cluster analysis. Atmos. Res. 197, 224–231. https://doi.org/10.1016/j.atmosres.2017.06.031.

Forsythe, N., Blenkinsop, S., Fowler, H.J., 2015. Exploring objective climate classification for the Himalayan arc and adjacent regions using gridded data sources. Earth Syst. Dyn. 6, 311–326. https://doi.org/10.5194/esd-6-311-2015.

Gallardo, C., Gil, V., Hagel, E., Tejeda, C., de Castro, M., 2013. Assessment of climate change in Europe from an ensemble of regional climate models by the use of Köppen–Trewartha classification. Int. J. Climatol. 33, 2157–2166. https://doi.org/10.1002/joc.3580.

Geiger, R., 1961. Überarbeitete Neuausgabe von Geiger, R.: Köppen- Geiger/Klima der Erde. (Wandkarte 1:16 Mill.). Klett- Perthes, Gotha.

Giorgetta, M.A., Jungclaus, J., Reick, C.H., Legutke, S., Bader, J., Böttinger, M., Brovkin, V., Crueger, T., Esch, M., Fieg, K., Glushak, K., Gayler, V., Haak, H., Hollweg, H.-D., Ilyina, T., Kinne, S., Kornblueh, L., Matei, D., Mauritsen, T., Mikolajewicz, U., Mueller, W., Notz, D., Pithan, F., Raddatz, T., Rast, S., Redler, R., Roeckner, E., Schmidt, H., Schnur, R., Segschneider, J., Six, K.D., Stockhause, M., Timmreck, C., Wegner, J., Widmann, H., Wieners, K.-H., Claussen, M., Marotzke, J., Stevens, B., 2013. Climate and carbon cycle changes from 1850 to 2100 in MPI-ESM simulations for the coupled model intercomparison project phase 5. J. Adv. Model. Earth Syst. 5, 572–597. https://doi.org/10.1002/jame.20038.

Giorgi, F., Gutowski, W.J., 2015. Regional dynamical downscaling and the CORDEX initiative. Annu. Rev. Environ. Resour. 40, 467–490. https://doi.org/10.1146/annurev-environ-102014-021217.

Giorgi, F., Coppola, E., Teichmann, C., Jacob, D., 2021. Editorial for the CORDEX-CORE experiment I special issue. Clim. Dyn. 57, 1265–1268. https://doi.org/10.1007/s00382-021-05902-w.

Gómez, G., Cabos, W.D., Liguori, G., Sein, D., Lozano-Galeana, S., Fita, L., Fernández, J., Magariño, M.E., Jiménez-Guerrero, P., Montávez, J.P., Domínguez, M., Romera, R., Gaertner, M.Á., 2016. Characterization of the wind speed variability and future change in the Iberian Peninsula and the Balearic Islands. Wind Energy 19, 1223–1237. https://doi.org/10.1002/we.1893.

Guisan, A., Zimmermann, N.E., 2000. Predictive habitat distribution models in ecology. Ecol. Model. 135, 147–186. https://doi.org/10.1016/S0304-3800(00)00354-9.

Hagemann, S., Dümenil-Gates, L., 1998. A parameterization of the lateral waterflow for the global scale. Clim. Dyn. 14, 17–31.

Hagemann, S., Gates, L.D., 2001. Validation of the hydrological cycle of ECMWF and NCEP reanalyses using the MPI hydrological discharge model. J. Geophys. Res. Atmos. 106, 1503–1510.

Hamed, M.M., Nashwan, M.S., Shahid, S., 2021. Inter-comparison of historical simulation and future projections of rainfall and temperature by CMIP5 and CMIP6 GCMs over Egypt. Int. J. Climatol. https://doi.org/10.1002/joc.7468.

Haylock, M.R., Hofstra, N., Klein Tank, A.M.G., Klok, E.J., Jones, P.D., New, M., 2008. A European daily high-resolution gridded data set of surface temperature and precipitation for 1950-2006. J. Geophys. Res. Atmos. 113 https://doi.org/10.1029/2008JD010201.

Hersbach, H., Bell, B., Berrisford, P., Hirahara, S., Horányi, A., Muñoz-Sabater, J., Nicolas, J., Peubey, C., Radu, R., Schepers, D., Simmons, A., Soci, C., Abdalla, S., Abellan, X., Balsamo, G., Bechtold, P., Biavati, G., Bidlot, J., Bonavita, M., De Chiara, G., Dahlgren, P., Dee, D., Diamantakis, M., Dragani, R., Flemming, J., Forbes, R., Fuentes, M., Geer, A., Haimberger, L., Healy, S., Hogan, R.J., Hólm, E., Janisková, M., Keeley, S., Laloyaux, P., Lopez, P., Lupu, C., Radnoti, G., de Rosnay, P., Rozum, I., Vamborg, F., Villaume, S., Thépaut, J.N., 2020. The ERA5 global reanalysis. Q. J. R. Meteorol. Soc. 146, 1999–2049. https://doi.org/10.1002/qj.3803.

Hibler, W.D., 1979. A dynamic thermodynamic sea ice model. J. Phys. Oceanogr. 9, 815–846.

Hirschi, M., Seneviratne, S.I., Alexandrov, V., Boberg, F., Boroneant, C., Christensen, O. B., Formayer, H., Orlowsky, B., Stepanek, P., 2011. Observational evidence for soil-moisture impact on hot extremes in southeastern Europe. Nat. Geosci. 4, 17–21.

Hofstra, N., Haylock, M., New, M., Jones, P.D., 2009. Testing E-OBS European high-resolution gridded data set of daily precipitation and surface temperature. J. Geophys. Res. Atmos. 114 https://doi.org/10.1029/2009JD011799.

Jacob, D., 2001. A note to the simulation of the annual and inter-annual variability of the water budget over the Baltic Sea drainage basin. Meteorog. Atmos. Phys. 77, 61–73. https://doi.org/10.1007/s007030170017.

Jacob, D., Petersen, J., Eggert, B., Alias, A., Christensen, O.B., Bouwer, L.M., Braun, A., Colette, A., Déqué, M., Georgievski, G., Georgopoulou, E., Gobiet, A., Menut, L., Nikulin, G., Haensler, A., Hempelmann, N., Jones, C., Keuler, K., Kovats, S., Kröner, N., Kotlarski, S., Kriegsmann, A., Martin, E., van Meijgaard, E., Moseley, C., Pfeifer, S., Preuschmann, S., Radermacher, C., Radtke, K., Rechid, D., Rounsevell, M., Samuelsson, P., Somot, S., Soussana, J.F., Teichmann, C., Valentini, R., Vautard, R., Weber, B., Yiou, P., 2014. EURO-CORDEX: new high-resolution climate change projections for European impact research. Reg. Environ. Chang. 14, 563–578. https://doi.org/10.1007/s10113-013-0499-2.

Jacob, D., Teichmann, C., Sobolowski, S., Katragkou, E., Anders, I., Belda, M., Benestad, R., Boberg, F., Buonomo, E., Cardoso, R.M., Casanueva, A., Christensen, O. B., Christensen, J.H., Coppola, E., De Cruz, L., Davin, E.L., Dobler, A., Domínguez, M., Fealy, R., Fernandez, J., Gaertner, M.A., García-Díez, M., Giorgi, F., Gobiet, A., Goergen, K., Gómez-Navarro, J.J., Alemán, J.J.G., Gutiérrez, C., Gutiérrez, J.M., Güttler, I., Haensler, A., Halenka, T., Jerez, S., Jiménez-Guerrero, P., Jones, R.G., Keuler, K., Kjellström, E., Knist, S., Kotlarski, S., Maraun, D., van Meijgaard, E., Mercogliano, P., Montávez, J.P., Navarra, A., Nikulin, G., de Noblet-Ducoudré, N., Panitz, H.J., Pfeifer, S., Piazza, M., Pichelli, E., Pietikäinen, J.P., Prein, A.F., Preuschmann, S., Rechid, D., Rockel, B., Romera, R., Sánchez, E., Sieck, K., Soares, P.M.M., Somot, S., Srnec, L., Sørland, S.L., Termonia, P., Truhetz, H., Vautard, R., Warrach-Sagi, K., Wulfmeyer, V., 2020. Regional climate downscaling over Europe: perspectives from the EURO-CORDEX community. Reg. Environ. Chang. 20 https://doi.org/10.1007/s10113-020-01606-9.

Jacobeit, J., 2010. Classifications in climate research. Phys. Chem. Earth 35, 411–421. https://doi.org/10.1016/j.pce.2009.11.010.

Jiménez-Guerrero, P., Montávez, J.P., Dominguez, M., Romera, R., Fita, L., Fernández, J., Cabos, W.D., Liguori, G., Gaertner, M.A., 2013. Mean fields and interannual variability in RCM simulations over Spain: the ESCENA project. Clim. Res. 57, 201–220.

Jungclaus, J.H., Fischer, N., Haak, H., Lohmann, K., Marotzke, J., Matei, D., Mikolajewicz, U., Notz, D., Von Storch, J.S., 2013. Characteristics of the ocean simulations in the Max Planck Institute Ocean Model (MPIOM) the ocean component of the MPI-Earth system model. J. Adv. Model. Earth Syst. 5, 422–446. https://doi.org/10.1002/jame.20023.

Jylhä, K., Tuomenvirta, H., Ruosteenoja, K., Niemi-Hugaerts, H., Keisu, K., Karhu, J.A., 2010. Observed and projected future shifts of climatic zones in Europe and their use to visualize climate change information. Weather. Clim. Soc. 2, 148–167. https://doi.org/10.1175/2010WCAS1010.1.

Keller, J.D., Wahl, S., 2021. Representation of climate in reanalyses: an intercomparison for Europe and North America. J. Clim. 34, 1667–1684. https://doi.org/10.1175/JCLI-D-20-0609.1.

Klemp, J.B., Durran, D.R., 1983. An upper boundary condition permitting internal gravity wave radiation in numerical mesoscale models. Mon. Weather Rev. 111, 430–444.

Komurcu, M., Emanuel, K.A., Huber, M., Acosta, R.P., 2018. High-resolution climate projections for the Northeastern United States using dynamical downscaling at convection-permitting scales. Earth Sp. Sci. 5, 801–826. https://doi.org/10.1029/2018EA000426.

Köppen, W., 1936. Das geographische System der Klimate. Handb. der Klimatologie 7–30. https://doi.org/10.3354/cr01204.

Kottek, M., Grieser, J., Beck, C., Rudolf, B., Rubel, F., 2006. World map of the Köppen-Geiger climate classification updated. Meteorol. Z. 15, 259–263. https://doi.org/10.1127/0941-2948/2006/0130.

Kücken, M., Gerstengarbe, F.-W., Orlowsky, B., 2009. A combination of cluster analysis and kappa statistic for the evaluation of climate model results. J. Appl. Meteorol. Climatol. 48, 1757–1765. https://doi.org/10.1175/2009JAMC2083.1.

Lavender, S.L., Walsh, K.J.E., Utembe, S., Caron, L.P., Guishard, M., 2021. Estimation of maximum seasonal tropical cyclone damage in the Atlantic using climate models. Nat. Hazards. https://doi.org/10.1007/s11069-021-04977-2.

Lohmann, U., Sausen, R., Bengtsson, L., Cubasch, U., Perlwitz, J., Roeckner, E., 1993. The Koppen climate classification as a diagnostic tool for general circulation models. Clim. Res. 3, 177–193.

Lorenz, R., Stalhandske, Z., Fischer, E.M., 2019. Detection of a climate change signal in extreme heat, heat stress, and cold in Europe from observations. Geophys. Res. Lett. 46, 8363–8374. https://doi.org/10.1029/2019GL082062.

Maier-Reimer, E., Kriest, I., Segschneider, J., Wetzel, P., 2005. The Hamburg Ocean Carbon Cycle Model hamocc5. 1-Technical Description Release 1.1.

Majewski, D., 1991. The Europa–Modell of the Deutscher Wetterdienst. ECMWF Seminar on Numerical Methods in Atmospheric Models, vol. 2. Eur. Cent. Mediu. Range Weather Forecast, Reading, UK, pp. 147–191.

Marsland, S.J., Haak, H., Jungclaus, J.H., Latif, M., Röske, F., 2003. The Max-Planck-Institute global ocean/sea ice model with orthogonal curvilinear coordinates. Ocean Model 5, 91–127.

Mathis, M., Mayer, B., Pohlmann, T., 2013. An uncoupled dynamical downscaling for the North Sea: method and evaluation. Ocean Model 72, 153–166. https://doi.org/10.1016/j.ocemod.2013.09.004.

Metzger, M.J., Bunce, R.G.H., Jongman, R.H.G., Sayre, R., Trabucco, A., Zomer, R., 2013. A high-resolution bioclimate map of the world: a unifying framework for global biodiversity research and monitoring. Glob. Ecol. Biogeogr. 22, 630–638. https://doi.org/10.1111/geb.12022.

Monserud, R.A., Leemans, R., 1992. Comparing global vegetation maps with the Kappa statistic. Ecol. Model. 62, 275–293. https://doi.org/10.1016/0304-3800(92)90003-W.

Parras-Berrocal, I.M., Vazquez, R., Cabos, W., Sein, D., Manañes, R., Perez-Sanz, J., Izquierdo, A., 2020. The climate change signal in the Mediterranean Sea in a regionally coupled atmosphere-ocean model. Ocean Sci. 16, 743–765. https://doi.org/10.5194/os-16-743-2020.

Pontoppidan, M., Reuder, J., Mayer, S., Kolstad, E.W., 2017. Downscaling an intense precipitation event in complex terrain: the importance of high grid resolution. Tellus Ser. A Dyn. Meteorol. Oceanogr. 69 https://doi.org/10.1080/16000870.2016.1271561.

Qiu, Y., Feng, J., Yan, Z., Wang, J., Li, Z., 2021. High-resolution dynamical downscaling for regional climate projection in Central Asia based on bias-corrected multiple GCMs. Clim. Dyn. https://doi.org/10.1007/s00382-021-05934-2.

Rechid, D., Jacob, D., 2006. Influence of monthly varying vegetation on the simulated climate in Europe. Meteorol. Z. 15, 99–116.

Rockel, B., 2015. The regional downscaling approach: a brief history and recent advances. Curr. Clim. Chang. Rep. 1, 22–29. https://doi.org/10.1007/s40641-014-0001-3.

Roeckner, E., Arpe, K., Bengtsson, L., Christoph, M., Claussen, M., Dümenil, L., Esch, M., Giorgetta, M.A., Schlese, U., Schulzweida, U., 1996. The Atmospheric General Circulation Model ECHAM-4: Model Description and Simulation of Present-Day Climate. Max Planck Institute for Meteorology, Hamburg, Report, p. 218.

Roeckner, E., Bäuml, G., Bonaventura, L., Brokopf, R., Esch, M., Giorgetta, M., Hagemann, S., Kirchner, I., Kornblueh, L., Manzini, E., Rhodin, A., Schlese, U., Schulzweida, U., Tompkins, A., 2003. The Atmospheric General Circulation Model ECHAM 5. PART I: Model Description. Max Planck Institute for Meteorology, Hamburg, p. 349. Report.

Rubel, F., Kottek, M., 2010. Observed and projected climate shifts 1901-2100 depicted by world maps of the Köppen-Geiger climate classification. Meteorol. Z. 19, 135–141. https://doi.org/10.1127/0941-2948/2010/0430.

Rubel, F., Brugger, K., Haslinger, K., Auer, I., 2017. The climate of the European Alps: shift of very high resolution Köppen-Geiger climate zones 1800-2100. Meteorol. Z. 26, 115–125. https://doi.org/10.1127/metz/2016/0816.

Rummukainen, M., 2016. Added value in regional climate modeling. Wiley Interdiscip. Rev. Clim. Chang. 7, 145–159. https://doi.org/10.1002/wcc.378.

Sein, D.V., Mikolajewicz, U., Gröger, M., Fast, I., Cabos, W., Pinto, J.G., Hagemann, S., Semmler, T., Izquierdo, A., Jacob, D., 2015. Regionally coupled atmosphere-ocean-sea ice-marine biogeochemistry model ROM: 1. Description and validation. J. Adv. Model. Earth Syst. 7, 268–304. https://doi.org/10.1002/2014MS000357.

Sein, D.V., Gröger, M., Cabos, W., Alvarez-Garcia, F.J., Hagemann, S., Pinto, J.G., Izquierdo, A., et al., 2020. Regionally coupled atmosphere-ocean-marine biogeochemistry model ROM: 2. Studying the climate change signal in the North Atlantic and Europe. J. Adv. Model. Earth Syst. 12 (8), 2020.

Skalák, P., Farda, A., Zahradníček, P., Trnka, M., Hlásny, T., Štěpánek, P., 2018. Projected shift of Köppen–Geiger zones in the central Europe: a first insight into the implications for ecosystems and the society. Int. J. Climatol. 38, 3595–3606. https://doi.org/10.1002/joc.5520.

Szabó-Takács, B., Farda, A., Skalák, P., Meitner, J., 2019. Influence of bias correction methods on simulated köppen-Geiger climate zones in Europe. Climate 7, 1–24. https://doi.org/10.3390/cli7020018.

Takemi, T., Ito, R., 2020. Benefits of high-resolution downscaling experiments for assessing strong wind hazard at local scales in complex terrain: a case study of Typhoon Songda (2004). Prog. Earth Planet. Sci. 7, 1–16. https://doi.org/10.1186/s40645-019-0317-7.

Tapiador, F.J., Moreno, R., Navarro, A., 2019a. Consensus in climate classifications for present climate and global warming scenarios. Atmos. Res. 216, 26–36.

Tapiador, F.J., Moreno, R., Navarro, A., Sánchez, J.L., García-Ortega, E., 2019b. Climate classifications from regional and global climate models: performances for present climate estimates and expected changes in the future at high spatial resolution. Atmos. Res. 228, 107–121. https://doi.org/10.1016/j.atmosres.2019.05.022.

Thornthwaite, C.W., 1948. An approach toward a rational classification of climate. Geogr. Rev. 38, 55–94.

Tiwari, P.R., Kar, S.C., Mohanty, U.C., Dey, S., Sinha, P., Raju, P.V.S., Shekhar, M.S., 2014. Dynamical downscaling approach for wintertime seasonal-scale simulation over the Western Himalayas. Acta Geophys. 62, 930–952. https://doi.org/10.2478/s11600-014-0215-8.

Tonietto, J., Carbonneau, A., 2004. A multicriteria climatic classification system for grape-growing regions worldwide. Agric. For. Meteorol. 124, 81–97. https://doi.org/10.1016/j.agrformet.2003.06.001.

Trewartha, G.T., Horn, L.H., 1980. An Introduction to Climate, 5th ed. McGraw-Hill, New York.

Valcke, S., 2013. The OASIS3 coupler: a European climate modelling community software. Geosci. Model Dev. 6, 373–388.

Wan, K.K.W., Li, D.H.W., Yang, L., Lama, J.C., 2010. Climate classifications and building energy use implications in China. Energy Build. 42, 1463–1471. https://doi.org/10.1016/j.enbuild.2010.03.016.

Wang, W., Anderson, B.T., Kaufmann, R.K., Myneni, R.B., 2004. The relation between the North Atlantic Oscillation and SSTs in the North Atlantic basin. J. Clim. 17, 4752–4759.

Willmes, C., Becker, D., Brocks, S., Hütt, C., Bareth, G., 2017. High resolution Köppen-Geiger classifications of paleoclimate simulations. Trans. GIS 21, 57–73. https://doi.org/10.1111/tgis.12187.

Xu, Z., Rhoades, A.M., Johansen, H., Ullrich, P.A., Collins, W.D., 2018. An intercomparison of GCM and RCM dynamical downscaling for characterizing the hydroclimatology of California and Nevada. J. Hydrometeorol. 19, 1485–1506. https://doi.org/10.1175/JHM-D-17-0181.1.

Xue, Y., Janjic, Z., Dudhia, J., Vasic, R., De Sales, F., 2014. A review on regional dynamical downscaling in intraseasonal to seasonal simulation/prediction and major factors that affect downscaling ability. Atmos. Res. 147–148, 68–85. https://doi.org/10.1016/j.atmosres.2014.05.001.

Zeroual, A., Assani, A.A., Meddi, M., Alkama, R., 2019. Assessment of climate change in Algeria from 1951 to 2098 using the Köppen–Geiger climate classification scheme. Clim. Dyn. 52, 227–243. https://doi.org/10.1007/s00382-018-4128-0.

Zscheischler, J., Mahecha, M.D., Harmeling, S., 2012. Climate classifications: the value of unsupervised clustering. Procedia Comput. Sci. 9, 897–906. https://doi.org/10.1016/j.procs.2012.04.096.